

UNCLASSIFIED

Defense Technical Information Center  
Compilation Part Notice

ADP012082

TITLE: Multiphase CFD Modeling of Developed and Supercavitating Flows

DISTRIBUTION: Approved for public release, distribution unlimited

This paper is part of the following report:

TITLE: Supercavitating Flows [les Ecoulements supercavitants]

To order the complete compilation report, use: ADA400728

The component part is provided here to allow users access to individually authored sections of proceedings, annals, symposia, etc. However, the component should be considered within the context of the overall compilation report and not as a stand-alone technical report.

The following component part numbers comprise the compilation report:  
ADP012072 thru ADP012091

UNCLASSIFIED

# Multiphase CFD Modeling of Developed and Supercavitating Flows

Robert F. Kunz

Jules W. Lindau

Michael L. Billet

David R. Stinebring

The Pennsylvania State University Applied Research Laboratory

PO Box 30

University Park, PA 16804

USA

## Abstract

Engineering interest in natural and ventilated cavities about submerged bodies and in turbomachinery has led researchers to study and attempt to model large scale cavitation for decades. Comparatively simple analytical methods have been used widely and successfully to model developed cavitation, since the hydrodynamics of these flows are often dominated by irrotational and rotational inviscid effects. However, a range of more complex physical phenomena are often associated with such cavities, including viscous effects, unsteadiness, mass transfer, three-dimensionality and compressibility. Though some of these complicating physics can be accommodated in simpler physical models, the ongoing maturation and increased generality of multiphase Computational Fluid Dynamic (CFD) methods has motivated recent research by a number of groups in the application of these methods for developed cavitation analysis. This paper focuses on the authors' recent research activities in this area.

The authors have developed an implicit algorithm for the computation of viscous two-phase flows. The baseline differential equation system is the multi-phase Navier-Stokes equations, comprised of the mixture volume, mixture momentum and constituent volume fraction equations. Though further generalization is straightforward, a three-species formulation is pursued here, which separately accounts for the liquid and vapor (which exchange mass) as well as a non-condensable gas field. The implicit method developed employs a dual-time, preconditioned, three-dimensional algorithm, with multi-block and parallel execution capabilities. Time-derivative preconditioning is employed to ensure well-conditioned eigenvalues, which is important for the computational efficiency of the method. Special care is taken to ensure that the resulting eigensystem is independent of the density ratio and the local volume fraction, which renders the scheme well-suited to high density ratio, largely phase-separated two-phase flows characteristic of developed and supercavitating systems. A dual-time formulation is employed to accommodate the inherently unsteady physics of developed and super-cavities. We have recently extended the formulation for compressible constituents to accommodate analysis of high speed projectiles and rocket plumes, and these formulation elements are also summarized. To demonstrate the validation status and general capabilities of the scheme, numerous examples are presented.

## Nomenclature

### Symbols

$A_j$	flux Jacobians
$C_\mu, C_1, C_2$	turbulence model constants
$C_{dest}, C_{prod}$	mass transfer model constants
$C_i$	pseudo-sound speed
$C_p$	pressure coefficient
$C_D$	drag coefficient
$D$	source Jacobian

$d$	body diameter
$d_m$	bubble diameter
$e$	total energy per unit volume
$E, F, G$	flux vectors
$f$	frequency
$g_i$	gravity vector
$h$	enthalpy
$H$	source vector
$I$	identity matrix
$J$	metric Jacobian
$K_j$	transform matrix
$k$	turbulent kinetic energy
$L$	bubble length
$M, M_j +$	Mach number, similarity transform matrices
$m, \dot{m}$	mass transfer rates
$P$	turbulent kinetic energy production
$Pr_{tk}, Pr_{te}$	turbulent Prandtl numbers for $k$ and $\epsilon$
$p$	pressure
$Q$	transport variable vector
$Re$	Reynolds number
$Str$	Strouhal number
$s$	arc length along configuration
$t, t_\infty$	time coordinate, mean flow time scale ( $d/U_\infty$ )
$U_j$	velocity magnitude, contravariant velocity components
$u_i, u, v, w$	Cartesian velocity components
$x_i$	Cartesian coordinates
$Y$	mass fraction
$\alpha$	volume fraction, angle-of-attack
$\beta$	preconditioning parameter
$\Gamma, \Gamma_e$	time derivative preconditioning and transform matrices
$\epsilon$	turbulence dissipation rate, numerical Jacobian
	parameter, internal energy per unit mass
$\kappa, \phi$	MUSCL parameters
$\Lambda_j, \lambda_j$	eigenvalues
$\mu$	molecular viscosity
$\rho$	density
$\sigma$	cavitation number
$\tau$	pseudo-time coordinate
$v$	dissipation sensor
$\xi_j$	curvilinear coordinates

### Subscripts, Superscripts

$l\phi$	single-phase value
$i, j$	coordinate indices
$k$	constituent index, pseudo-time-step index
$L, R$	dependent variable values on left and right of face
$l$	liquid
$m$	mixture
$ng$	non-condensable gas
$t$	turbulent
$v$	condensable vapor, viscous
$\infty$	free stream value
$\hat{\phantom{x}}$	transformed to curvilinear coordinates
$+/-$	production/destruction, right/left running
$\sim$	with respect to mixture
$Y$	mass fraction form

## Introduction

Multi-phase flows have received growing research attention among CFD practitioners due in large measure to the evolving maturity of single-phase algorithms that have been adapted to the increased complexity of multi-component systems. However, there remain a number of numerical and physical modeling challenges that arise in multi-phase CFD analysis beyond those present in single-phase methods. Principal among these are large constituent density ratios, the presence of discrete interfaces, significant mass transfer rates, non-equilibrium interfacial dynamics, compressibility effects associated with the very low mixture sound speeds which can arise, the presence of multiple constituents (viz. more than two) and void wave propagation. These naturally deserve special attention when a numerical method is constructed or adapted for multi-phase flows.

The class of multiphase flows under consideration here is developed- and super-cavitating flows, wherein significant regions of the flow are occupied by gas phase. Depending on the configuration, such “developed” [38] cavities are composed of vapor and/or injected non-condensable gas.

Historically, most efforts to model large cavities relied on potential flow methods applied to the liquid flow, while the bubble shape and closure conditions were specified. Adaptations of potential flow methods remain in widespread use today ([15]), due to their inherent computational efficiency, and their proven effectiveness in predicting numerous first order dynamics of supercavitating configurations.

Recently, more general CFD approaches have been developed to analyze these flows. In one class of methods, a single continuity equation is considered with the density varying abruptly between vapor and liquid densities through an equation of state. Such “single-continuity-equation-homogeneous” methods have become fairly widely used for sheet and supercavitation analysis ([8], [9], [25], [35], [43], for example). Although these methods can directly model viscous effects, they are inherently unable to distinguish between condensable vapor and non-condensable gas, a requirement of ventilated supercavitating vehicle analysis.

By solving separate continuity equations for liquid and gas phase fields, one can account for and model the separate dynamics and thermodynamics of the liquid, condensable vapor, and non-condensable gas fields. Such multi-species methods are also termed homogeneous because interfacial dynamics are neglected, that is, there is assumed to be no-slip between constituents residing in the same control volume. A number of researchers have adopted this level of differential modeling, mostly for the analysis of natural cavitation where two phases/constituents are accounted for ([1], [23], [32], for example). This is the level of modeling employed here, though a three-species formulation is used to account for two gaseous fields. For two phases/constituents these methods are very closely related to the “single-continuity-equation-homogeneous” methods addressed above with interfacial mass transfer modeling supplanting an equation of state.

Full-two-fluid modeling, wherein separate momentum (and in principle energy) equations are employed for the liquid and vapor constituents, have also been utilized for natural cavitation [12]. However, in sheet-cavity flows, the gas-liquid interface is known to be nearly in dynamic equilibrium; for this reason, we do not pursue a full two-fluid level of modeling.

Sheet- and super-cavitating flows are characterized by large density ratios ( $\rho_l/\rho_v > 10^4$  is observed in near-atmospheric water applications), relatively discrete cavity-free stream interfaces and, due to ventilation, multiple gas phase constituents. Accordingly, the CFD method employed must accommodate these physics effectively.

Most relevant applications exhibit large scale unsteadiness associated with re-entrant jets, periodic ejection of non-condensable gas, and cavity “pulsations”. Accordingly, we and others ([23], [26], [32], [35], for example) employ a time-accurate formulation in the analysis of large scale cavitation.

## Compressibility

The compressibility of the liquid and gas phase constituents can significantly influence supercavitating flow configurations in three ways. First, regions of high gas volume fraction *bubbly* flow can exist if the cavity does not fully envelop the body, or if the cavitator is either poorly designed or operating off-design. In these circumstances the two-phase mixture can have a sound speed significantly lower than that of either liquid or gas constituents, as illustrated in Figure 1. This can affect hydrodynamic performance and gives rise to the cloud collapse physics responsible for cavitation damage.

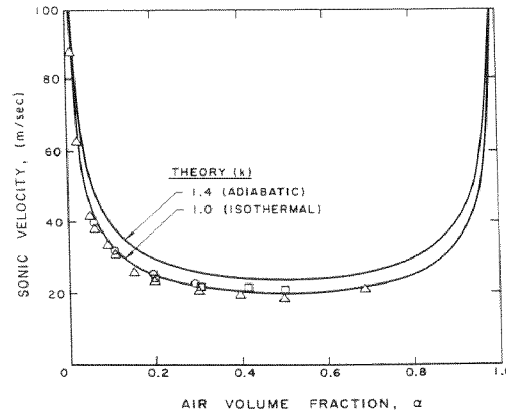


Figure 1. Variation of mixture sound speed in a bubbly air/water mixture. (From Brennan[4].)

The second compressibility issue arises in candidate rocket propulsion systems for very high speed underwater vehicles where exhaust velocities are supersonic (relative to propellant sound speed). Thirdly, very high speed underwater projectiles (i.e., unpropelled supercavitating darts) can be deployed at speeds which are supersonic with respect to the local sound speed of water. This application also requires a compressible CFD formulation ([30], for example). These compressibility effects have motivated several authors to employ compressible formulations ([1], [3], [30], [43] for example) and the present authors have recently extended our baseline formulation to accommodate compressible constituents.

The purpose of this paper is to present the numerical methods and physical models employed, and many of the applications pursued in the authors' research. The paper is organized as follows: The theoretical formulation of the method is summarized, including the baseline differential model, inviscid eigensystem, physical models, compressibility and key elements of the numerical method. Particular emphasis is placed on unique aspects of the numerics including the preconditioning strategy, resultant eigensystem characteristics, and flux evaluation and limiting strategies associated with the resolution of interfaces. This is followed by three sets of results. The first set includes axisymmetric steady-state and transient analyses of natural and ventilated cavitation about several configurations. These solutions are compared to experimental measurements to demonstrate the capability of the modeling employed. The second set of results includes a variety of three-dimensional analyses of sheet- and supercavitating flows of relevance to high speed vehicles and turbomachinery. The third set of results includes compressible simulations of a vehicle propulsion plume and a high speed supercavitating projectile.

## Theoretical Formulation

### Governing Equations

The baseline governing differential system employed is cast in Cartesian coordinates as:

$$\begin{aligned}
& \left( \frac{1}{\rho_m \beta^2} \right) \frac{\partial p}{\partial \tau} + \frac{\partial u_j}{\partial x_j} = (\dot{m}^+ + \dot{m}^-) \left( \frac{1}{\rho_l} - \frac{1}{\rho_v} \right) \\
& \frac{\partial}{\partial t} (\rho_m u_i) + \frac{\partial}{\partial \tau} (\rho_m u_i) + \frac{\partial}{\partial x_j} (\rho_m u_i u_j) = \\
& \quad - \frac{\partial p}{\partial x_i} + \frac{\partial}{\partial x_j} \left( \mu_{m,t} \left[ \frac{\partial u_i}{\partial x_j} + \frac{\partial u_j}{\partial x_i} \right] \right) + \rho_m g_i \\
& \frac{\partial \alpha_l}{\partial t} + \left( \frac{\alpha_l}{\rho_m \beta^2} \right) \frac{\partial p}{\partial \tau} + \frac{\partial \alpha_l}{\partial \tau} + \frac{\partial}{\partial x_j} (\alpha_l u_j) = (\dot{m}^+ + \dot{m}^-) \left( \frac{1}{\rho_l} \right) \\
& \frac{\partial \alpha_{ng}}{\partial t} + \left( \frac{\alpha_{ng}}{\rho_m \beta^2} \right) \frac{\partial p}{\partial \tau} + \frac{\partial \alpha_{ng}}{\partial \tau} + \frac{\partial}{\partial x_j} (\alpha_{ng} u_j) = 0 \quad ,
\end{aligned} \tag{1}$$

where  $\alpha_l$  and  $\alpha_{ng}$  represent the liquid phase and non-condensable gas volume fractions, and mixture density and mixture turbulent viscosity are defined as:

$$\begin{aligned}
\rho_m &\equiv \rho_l \alpha_l + \rho_v \alpha_v + \rho_{ng} \alpha_{ng} \\
\mu_{m,t} &= \frac{\rho_m C_\mu k^2}{\varepsilon}
\end{aligned} \tag{2}$$

In this *baseline* formulation, the density of each constituent is taken as constant. The mass transfer rates from vapor to liquid and from liquid to vapor are denoted  $\dot{m}^+$  and  $\dot{m}^-$ , respectively. Mass transfer terms appear in the mixture continuity equation because this equation is a statement of mixture volume conservation. Also, note that each of the equations contains two sets of time-derivatives - those written in terms of the variable “t” correspond to physical time terms, while those written in terms of “ $\tau$ ” correspond to pseudo-time terms that are employed in the time-iterative solution procedure. The forms of the pseudo-time terms will be discussed presently.

In the development of the differential system presented above, a number of physical, numerical, and practical issues were considered. First, a mixture *volume* continuity equation is employed rather than a mixture mass equation. This initial choice was made based on the authors’ experience that the *nonlinear* performance of segregated pressure based algorithms [17] is improved by doing so for high density ratio multi-phase systems. Because of this choice, neither a physical time derivative nor mixture density appears in the continuity equation, although the mixture density can vary in space and time. To render the system hyperbolic and to facilitate the use of time-marching procedures, we then introduce a pseudo-time derivative term (signified by “ $\tau$ ”) in the mixture continuity equation, a strategy that derives from the work of Chorin [7] and others.

Second, corresponding artificial time-derivative terms are also introduced in the component phasic continuity equations, which ensures that the proper differential equation (in non-conservative form) is satisfied. That is, combining equations [1]a and [1]c:

$$\begin{aligned}
& \frac{\partial \alpha_l}{\partial t} + \left( \frac{\alpha_l}{\rho_m \beta^2} \right) \frac{\partial p}{\partial \tau} + \frac{\partial \alpha_l}{\partial \tau} + \frac{\partial}{\partial x_j} (\alpha_l u_j) = \\
& \frac{\partial \alpha_l}{\partial t} + \left( \frac{\alpha_l}{\rho_m \beta^2} \right) \frac{\partial p}{\partial \tau} + \frac{\partial \alpha_l}{\partial \tau} + \alpha_l \left( \frac{-1}{\rho_m \beta^2} \right) \frac{\partial p}{\partial \tau} + u_j \frac{\partial \alpha_l}{\partial x_j} = \\
& \frac{\partial \alpha_l}{\partial t} + \frac{\partial \alpha_l}{\partial \tau} + u_j \frac{\partial \alpha_l}{\partial x_j} \equiv 0
\end{aligned} \tag{3}$$

Inclusion of such “phasic continuity enforcing” terms has a favorable impact on the nonlinear performance of multi-phase algorithms when mass transfer is present [34].

Third, we desired an eigensystem that is independent of density ratio and volume fractions so that the performance of the algorithm would be commensurate with that of single-phase for a wide range of multi-phase conditions. These considerations give rise to the preconditioned system in equation [1].

In generalized coordinates, equations [1] can be written in vector form as:

$$\Gamma_e \frac{\partial}{\partial t} \hat{Q} + \Gamma \frac{\partial}{\partial \tau} \hat{Q} + \frac{\partial \hat{E}_j}{\partial \xi_j} - \frac{\partial \hat{E}_j^v}{\partial \xi_j} - \hat{H} = 0, \quad (4)$$

where the primitive solution variable, flux, and source vectors are written:

$$\begin{aligned} \hat{Q} &= JQ = J(p, u_i, \alpha_l, \alpha_{ng})^T \\ \hat{E}_j &= J(U_j, \rho_m u_i U_j + \xi_{j,i} p, \alpha_l U_j, \alpha_{ng} U_j)^T \\ \hat{E}_j^v &= J\left(0, \mu_{m,t}(\nabla \xi_j \cdot \nabla \xi_j) \frac{\partial u_i}{\partial \xi_j} + \xi_{j,i} \frac{\partial u_k}{\partial \xi_j} \xi_{j,k}, 0, 0\right)^T \\ \hat{H} &= J\left((\dot{m}^+ + \dot{m}^-) \left(\frac{1}{\rho_l} - \frac{1}{\rho_v}\right), \rho_m g_i, (\dot{m}^+ + \dot{m}^-) \left(\frac{1}{\rho_l}\right), 0\right)^T, \end{aligned} \quad (5)$$

and  $J$  is the metric Jacobian,  $J \equiv \partial(x, y, z)/\partial(\xi, \eta, \zeta)$ .

Matrix  $\Gamma_e$  is defined by:

$$\Gamma_e \equiv \begin{bmatrix} 0 & 0 & 0 & 0 & 0 & 0 \\ 0 & \rho_m & 0 & 0 & u\Delta\rho_1 & u\Delta\rho_2 \\ 0 & 0 & \rho_m & 0 & v\Delta\rho_1 & v\Delta\rho_2 \\ 0 & 0 & 0 & \rho_m & w\Delta\rho_1 & w\Delta\rho_2 \\ 0 & 0 & 0 & 0 & 1 & 0 \\ 0 & 0 & 0 & 0 & 0 & 1 \end{bmatrix}, \quad (6)$$

and the preconditioning matrix,  $\Gamma$ , takes the form:

$$\Gamma \equiv \begin{bmatrix} \left(\frac{1}{\rho_m \beta^2}\right) & 0 & 0 & 0 & 0 & 0 \\ 0 & \rho_m & 0 & 0 & u\Delta\rho_1 & u\Delta\rho_2 \\ 0 & 0 & \rho_m & 0 & v\Delta\rho_1 & v\Delta\rho_2 \\ 0 & 0 & 0 & \rho_m & w\Delta\rho_1 & w\Delta\rho_2 \\ \left(\frac{\alpha_l}{\rho_m \beta^2}\right) & 0 & 0 & 0 & 1 & 0 \\ \left(\frac{\alpha_{ng}}{\rho_m \beta^2}\right) & 0 & 0 & 0 & 0 & 1 \end{bmatrix} \quad (7)$$

where  $\Delta\rho_1 \equiv \rho_l - \rho_v$  and  $\Delta\rho_2 \equiv \rho_{ng} - \rho_v$ . The compatibility condition,  $\alpha_l + \alpha_v + \alpha_{ng} = 1$ , is incorporated implicitly in definitions 6 and 7.

## Eigensystem

Of interest in the construction and analysis of a scheme to discretize and solve equation [4] is its inviscid eigensystem. In particular, the eigenvalues and eigenvectors of matrix  $\tilde{A}_j$  are required, where

$$\tilde{A}_j \equiv \Gamma^{-1} A_j, \quad A_j \equiv \frac{\partial \hat{E}_j}{\partial \hat{Q}}. \quad (8)$$

$A_j$ ,  $\Gamma^{-1}$ , and  $\tilde{A}_j$  can be computed straightforwardly, and expressions for these are available in [18]. The eigenvalues and eigenvectors of  $\tilde{A}_j$  can be found by first considering the reduction of equation [4] to a single-phase system. With  $\alpha_l = 1$ ,  $\rho_m = \rho_l = \rho_v = \rho_{ng}$  (= constant),  $\dot{m}^{+/-} = 0$ , equation [4] collapses to the widely used single-phase “pseudo-compressibility” scheme, which can be written for inviscid flow as

$$\begin{aligned} \frac{\partial \hat{Q}^{1\phi}}{\partial t} + \frac{\partial \hat{E}_j^{1\phi}}{\partial \xi_j} &= 0 \\ \hat{Q}^{1\phi} &= J(p, u_i)^T \\ \hat{E}_j^{1\phi} &= (U_j, u_i U_j + \xi_{j,i} p)^T \\ A_j^{1\phi} &\equiv \frac{\partial \hat{E}_j^{1\phi}}{\partial \hat{Q}^{1\phi}}. \end{aligned} \quad (9)$$

Flux Jacobian matrix  $A_j^{1\phi}$  has a well known form ([28], for example) and is also given in [18].

Comparing the expressions for  $A_j^{1\phi}$  and  $\tilde{A}_j$ , one can write:

$$\tilde{A}_j = \begin{bmatrix} K^{-1} \{A_j^{1\phi}\} K & 0 & 0 \\ 0 & U_j & 0 \\ 0 & 0 & U_j \end{bmatrix}, K \equiv \begin{bmatrix} 1 & 0 \\ \rho_m & 0 \\ 0 & I \end{bmatrix}. \quad (10)$$

Diagonalizing  $\tilde{A}_j$ :

$$\tilde{A}_j = M_j \Lambda_j M_j^{-1}. \quad (11)$$

The elements of the diagonal matrix  $\Lambda_j$  are the eigenvalues of  $\tilde{A}_j$ . Similarity transform matrices  $M_j$  and  $M_j^{-1}$  contain the right and left eigenvectors of  $\tilde{A}_j$ . Forms for these matrices are sought. Using equation [10], we can write equation [11] as

$$\begin{aligned} \begin{bmatrix} K^{-1} \{A_j^{1\phi}\} K & 0 & 0 \\ 0 & U_j & 0 \\ 0 & 0 & U_j \end{bmatrix} &= \begin{bmatrix} K^{-1} \{M_j^{1\phi}\} & 0 & 0 \\ 0 & 1 & 0 \\ 0 & 0 & 1 \end{bmatrix} \times \\ &\quad \begin{bmatrix} \{ \Lambda_j^{1\phi} \} & 0 & 0 \\ 0 & U_j & 0 \\ 0 & 0 & U_j \end{bmatrix} \begin{bmatrix} \{M_j^{1\phi}\} K & 0 & 0 \\ 0 & 1 & 0 \\ 0 & 0 & 1 \end{bmatrix}. \end{aligned} \quad (12)$$

This brief analysis illustrates that the inviscid eigenvalues of the present preconditioned multi-phase system



are the same as the standard single-phase pseudo-compressibility system with two additional eigenvalues introduced,  $U_j$ ,  $U_j$ . That is,

$$\Lambda_j = (U_j, U_j, U_j + C_j, U_j - C_j, U_j, U_j)^T$$

$$C_j = \sqrt{U_j^2 + \beta^2(\xi_{j,i}\xi_{j,i})}$$
(13)

Equation [12] also illustrates that a complete set of linearly independent eigenvectors exists for the present three-component system. These results generalize for an arbitrary number of constituents. The eigenvalues are seen to be independent of the volume fractions and density ratio. This is not the case for other choices of preconditioning matrix,  $\Gamma$ , or if a mixture mass conservation equation is chosen instead of the mixture volume equation.

The local time-steps and matrix dissipation operators presented below are derived from the inviscid multi-phase eigensystem above, which has been shown to be closely related to the known single-phase eigensystem. This has had the practical advantage of making the single-phase predecessor code easier to adapt to the multi-phase system.

## Physical Modeling

### Mass Transfer

For transformation of liquid to vapor,  $\dot{m}^-$  is modeled as being proportional to the liquid volume fraction and the amount by which the pressure is below the vapor pressure. This model is similar to that used by Merkle et al. [23] for both evaporation and condensation. For transformation of vapor to liquid,  $\dot{m}^+$ , a simplified form of the Ginzburg-Landau potential is employed:

$$\dot{m}^- = \frac{C_{\text{dest}} \rho_v \alpha_l \text{MIN}[0, p - p_v]}{(1/2 \rho_l U_\infty^2) t_\infty}$$

$$\dot{m}^+ = \frac{C_{\text{prod}} \rho_v (\alpha_l - \alpha_{\text{ng}})^2 (1 - \alpha_l - \alpha_{\text{ng}})}{t_\infty}$$
(14)

In this work,  $C_{\text{dest}}$  and  $C_{\text{prod}}$  are empirical constants (here  $C_{\text{dest}} = 10^5$ ,  $C_{\text{prod}} = 10^5$ ).  $\alpha_{\text{ng}}$  appears in the production term to enforce that  $\dot{m}^- \rightarrow 0$  as  $\alpha_v \rightarrow 0$ . Both mass transfer rates are non-dimensionalized with respect to a mean flow time scale.

The mass transfer model presented in equation [14] retains the physically observed characteristic that cavity sizes, and thereby the dynamics of the two-fluid motion, are nearly independent of liquid-vapor density ratio. One outcome of the eigensystem characteristics summarized above is that the numerical behavior of the code parallels this physical behavior. This is illustrated in Figure 2. There, the convergence histories are provided for six simulations of cavitating flow over a hemispherical forebody with cylindrical afterbody (1/2 caliber ogive,  $\sigma = 0.3$ , from series of results presented below). As the density ratio is increased from 1 to 10, the convergence history is modified somewhat, but beyond  $\rho_l/\rho_v = 10$ , the performance of the solver is virtually independent of density ratio up to  $\rho_l/\rho_v = 10^5$ . This behavior is consistent with the modeled physics of this problem as shown in Figure 3. There, drag coefficient and number of predicted vaporous cells are seen to reach a nearly constant value at  $\rho_l/\rho_v > 10$ .

As the authors have evolved this work into the analysis of turbomachinery, it has become evident that the present mass transfer model has some shortcomings in that it does not accommodate thermal effects on cavitation breakdown performance in turbomachinery [5]. This is discussed further in the pump cavitation results

section below.

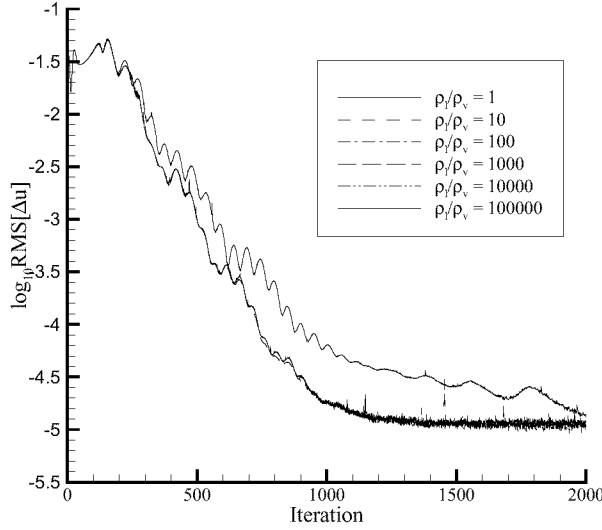


Figure 2. Comparison of convergence histories with density ratio for hemispherical forebody simulation.

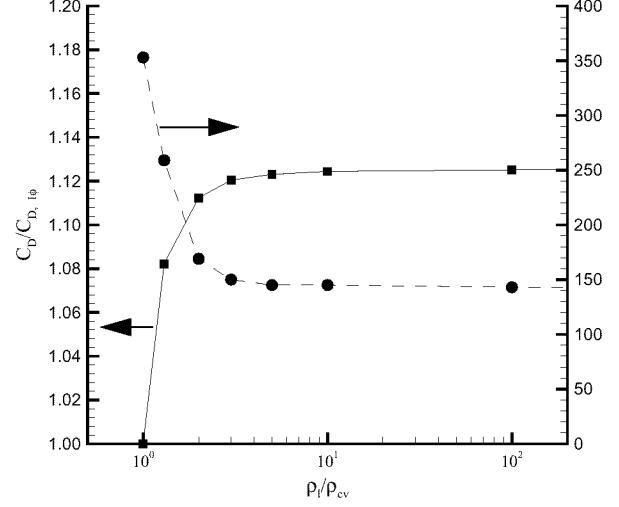


Figure 3. Comparison of predicted drag coefficient and number of vaporous cells with density ratio for hemispherical forebody simulation.

### Turbulence Closure

A high Reynolds number form  $k$ - $\epsilon$  model (Jones and Launder [16]) with standard wall functions is implemented to provide turbulence closure:

$$\frac{\partial}{\partial t}(\rho_m k) + \frac{\partial}{\partial x_j}(\rho_m k u_j) = \frac{\partial}{\partial x_j} \left( \frac{\mu_{m,t}}{\text{Pr}_{tk}} \frac{\partial k}{\partial x_j} \right) + P - \rho \epsilon \quad (15)$$

$$\frac{\partial}{\partial t}(\rho_m \epsilon) + \frac{\partial}{\partial x_j}(\rho_m \epsilon u_j) = \frac{\partial}{\partial x_j} \left( \frac{\mu_{m,t}}{\text{Pr}_{te}} \frac{\partial \epsilon}{\partial x_j} \right) + [C_1 P - C_2 \rho \epsilon] \left( \frac{\epsilon}{k} \right)$$

As with velocity, the turbulence scalars are interpreted as being mixture quantities. Other two-equation turbulence models have also been employed as discussed below.

### Compressible Constituent Phases

As mentioned above, a complicating phenomena associated with underwater multiphase flows is the presence and effect of compressibility in a flow that is largely incompressible. To directly model flows containing homogeneously mixed bubbly flow regions and/or shock-expansion wave systems, a suitable representation of compressible flow is necessary. Also, in flows of relevance here, liquid vapor mass transfer is important and by virtue of ventilation, a noncondensable gas phase is present.

For the purposes of analysis and development of appropriate preconditioning, the inviscid one-dimensional two-phase form of the governing equations are presented in equation [16]. Here, with no loss of generality, the equations are presented in mass-fraction form. In this form, the governing equations for two-phase flow resemble the equations employed in single-phase multi-component reacting-gas-mixture flows. The eigenvalues of the associated system and the preconditioning forms are well known and have been widely used [40]. The equations corresponding to a preferred set of primitive variables may be achieved and then interpreted in the context of multi-phase flows of interest. A more complete development with applications is given in references [20], [21] and [41].

### Compressible Equations of Motion

The fully compressible form of the two-phase equations in 1D is given as,

$$\frac{\partial Q_Y}{\partial \tau} + \frac{\partial E}{\partial x} = 0 \quad (16)$$

which represents the following set of equations in conservation form,

$$\frac{\partial \rho Y_v}{\partial \tau} + \frac{\partial \rho Y_v u}{\partial x} = 0 \quad (17)$$

$$\frac{\partial \rho Y_l}{\partial \tau} + \frac{\partial \rho Y_l u}{\partial x} = 0 \quad (18)$$

$$\frac{\partial \rho u}{\partial \tau} + \frac{\partial \rho u^2}{\partial x} + \frac{\partial p}{\partial x} = 0 \quad (19)$$

$$\frac{\partial e}{\partial \tau} + \frac{\partial (e + p)u}{\partial x} = 0 \quad (20)$$

The mixture density is defined as:

$$\rho = \tilde{\rho}_v + \tilde{\rho}_l = \rho_l \alpha_l + \rho_v \alpha_v \quad (21)$$

where,

$$\tilde{\rho}_v = \rho Y_v = \rho_v \alpha_v \quad \text{and} \quad \tilde{\rho}_l = \rho Y_l = \rho_l \alpha_l \quad (22)$$

The total internal energy of the two-phase mixture may be expressed as,

$$e = \rho e + \frac{1}{2} \rho u^2 = \rho h - p + \frac{1}{2} \rho u^2 \quad (23)$$

and the specific enthalpy of the mixture is given as,

$$h = \sum_{i=l,v} h_i Y_i \quad (24)$$

and  $h_l$  and  $h_v$  are the phasic enthalpies, which are also generally known functions of the temperature and the pressure. The  $\tilde{\rho}$  indicates where, in equations [21] and [22], the mass fraction based, Dalton model, of species density is to be used, rather than the volume fraction based, Amagat model. For development of the compressible preconditioning form, the Dalton model for intensive properties is used here.

The system in equations [17]-[20] may equivalently be expressed in the following vector form:

$$\tilde{\Gamma}_e \frac{\partial \tilde{Q}}{\partial \tau} + \frac{\partial E}{\partial x} = 0 \quad (25)$$

where we have adopted a set of primitive variables,  $\tilde{Q}$ , as the primary dependent vector:

$$\tilde{Q} = \begin{bmatrix} p \\ Y_v \\ u \\ T \end{bmatrix} \quad E = \begin{bmatrix} \rho Y_v u \\ \rho Y_l u \\ \rho u^2 + p \\ (e + p)u \end{bmatrix}$$

$$\tilde{\Gamma}_e = \begin{bmatrix} Y_v \frac{\partial \rho}{\partial p} \Big|_{\tilde{Q}} & \rho + Y_v \frac{\partial \rho}{\partial Y_v} \Big|_{\tilde{Q}} & 0 & Y_v \frac{\partial \rho}{\partial T} \Big|_{\tilde{Q}} \\ Y_l \frac{\partial \rho}{\partial p} \Big|_{\tilde{Q}} & -\rho + Y_l \frac{\partial \rho}{\partial Y_v} \Big|_{\tilde{Q}} & 0 & Y_l \frac{\partial \rho}{\partial T} \Big|_{\tilde{Q}} \\ u \frac{\partial \rho}{\partial p} \Big|_{\tilde{Q}} & u \frac{\partial \rho}{\partial Y_v} \Big|_{\tilde{Q}} & \rho & u \frac{\partial \rho}{\partial T} \Big|_{\tilde{Q}} \\ -\left(1 - \rho \frac{\partial h}{\partial p} \Big|_{\tilde{Q}}\right) + h_0 \frac{\partial \rho}{\partial p} \Big|_{\tilde{Q}} & \rho \frac{\partial h}{\partial Y_v} \Big|_{\tilde{Q}} + h_0 \frac{\partial \rho}{\partial Y_v} \Big|_{\tilde{Q}} & \rho u & \rho \frac{\partial h}{\partial T} \Big|_{\tilde{Q}} + h_0 \frac{\partial \rho}{\partial T} \Big|_{\tilde{Q}} \end{bmatrix}$$

The corresponding system flux Jacobian is defined as:

$$\tilde{A} = \begin{bmatrix} u Y_v \frac{\partial \rho}{\partial p} \Big|_{\tilde{Q}} & \rho u + u Y_v \frac{\partial \rho}{\partial Y_v} \Big|_{\tilde{Q}} & \rho Y_v & u Y_v \frac{\partial \rho}{\partial T} \Big|_{\tilde{Q}} \\ u Y_l \frac{\partial \rho}{\partial p} \Big|_{\tilde{Q}} & -\rho u + u Y_l \frac{\partial \rho}{\partial Y_v} \Big|_{\tilde{Q}} & \rho Y_l & u Y_l \frac{\partial \rho}{\partial T} \Big|_{\tilde{Q}} \\ 1 + u^2 \frac{\partial \rho}{\partial p} \Big|_{\tilde{Q}} & u^2 \frac{\partial \rho}{\partial Y_v} \Big|_{\tilde{Q}} & 2\rho u & u^2 \frac{\partial \rho}{\partial T} \Big|_{\tilde{Q}} \\ \rho u \frac{\partial h}{\partial p} \Big|_{\tilde{Q}} + u h_0 \frac{\partial \rho}{\partial p} \Big|_{\tilde{Q}} & \rho u \frac{\partial h}{\partial Y_v} \Big|_{\tilde{Q}} + u h_0 \frac{\partial \rho}{\partial Y_v} \Big|_{\tilde{Q}} & \rho(h_0 + u^2) & \rho u \frac{\partial h}{\partial T} \Big|_{\tilde{Q}} + u h_0 \frac{\partial \rho}{\partial T} \Big|_{\tilde{Q}} \end{bmatrix} \quad (26)$$

Note that a standard notation has been used to indicate partial differentiation with respect to the variables in  $\tilde{Q}$ . The eigenvalues of the above system are:

$$\lambda([\tilde{\Gamma}_e]^{-1} \tilde{A}) = u, u, u \pm c \quad (27)$$

where the speed of sound is given by:.

$$c^2 = \frac{\rho \frac{\partial h}{\partial T} \Big|_{\tilde{Q}}}{\rho \frac{\partial \rho}{\partial p} \Big|_{\tilde{Q}} \frac{\partial h}{\partial T} \Big|_{\tilde{Q}} + \frac{\partial \rho}{\partial T} \Big|_{\tilde{Q}} \left(1 - \rho \frac{\partial h}{\partial p} \Big|_{\tilde{Q}}\right)}$$

For the multi-phase system, the above partial derivatives need to be obtained in terms of the known volume fraction based properties, i.e.,  $\rho_v = \rho_v(p, T)$  and  $\rho_l = \rho_l(p, T)$ . Their evaluation is therefore not as straightforward as for single-phase multi-component mixtures.

The relation for the *isothermal* sound speed is given in equation [28].

$$\begin{aligned} \left. \frac{\partial \rho}{\partial p} \right|_{\tilde{Q}} &= \rho \left[ \frac{\alpha_l \partial \rho_L}{\rho_l \partial p} \right]_{\tilde{Q}} + \frac{\alpha_v \partial \rho_v}{\rho_v \partial p} \bigg|_{\tilde{Q}} \\ \frac{1}{c^2} \bigg|_T &= \left. \frac{\partial \rho}{\partial p} \right|_{\tilde{Q}} \end{aligned} \quad (28)$$

### Preconditioned Compressible Equations of Motion

The preconditioned version of equation [25] may be written as:

$$\tilde{\Gamma} \frac{\partial \tilde{Q}}{\partial \tau} + \frac{\partial E}{\partial x} = 0 \quad (29)$$

where the preconditioning matrix is given by:

$$\tilde{\Gamma} = \begin{bmatrix} Y_v \frac{\partial \rho'}{\partial p} \bigg|_{\tilde{Q}} & \rho + Y_v \frac{\partial \rho}{\partial Y_v} \bigg|_{\tilde{Q}} & 0 & Y_v \frac{\partial \rho}{\partial T} \bigg|_{\tilde{Q}} \\ Y_l \frac{\partial \rho'}{\partial p} \bigg|_{\tilde{Q}} & -\rho + Y_l \frac{\partial \rho}{\partial Y_v} \bigg|_{\tilde{Q}} & 0 & Y_l \frac{\partial \rho}{\partial T} \bigg|_{\tilde{Q}} \\ u \frac{\partial \rho'}{\partial p} \bigg|_{\tilde{Q}} & u \frac{\partial \rho}{\partial Y_v} \bigg|_{\tilde{Q}} & \rho & u \frac{\partial \rho}{\partial T} \bigg|_{\tilde{Q}} \\ -\left(1 - \rho \frac{\partial h}{\partial p} \bigg|_{\tilde{Q}}\right) + h_0 \frac{\partial \rho'}{\partial p} \bigg|_{\tilde{Q}} & \rho \frac{\partial h}{\partial Y_v} \bigg|_{\tilde{Q}} + h_0 \frac{\partial \rho}{\partial Y_v} \bigg|_{\tilde{Q}} & \rho u \rho \frac{\partial h}{\partial T} \bigg|_{\tilde{Q}} + h_0 \frac{\partial \rho}{\partial T} \bigg|_{\tilde{Q}} \end{bmatrix} \quad (30)$$

The eigenvalues of the preconditioned system can be shown to be:

$$\lambda(\tilde{\Gamma}^{-1} A) = u, u, \frac{1}{2} \left[ u \left( 1 + \left( \frac{c'}{c} \right)^2 \right) \pm \sqrt{u^2 \left( 1 - \left( \frac{c'}{c} \right)^2 \right)^2 + 4c'^2} \right] \quad (31)$$

where the preconditioned pseudo-sound-speed is:

$$(c')^2 = \frac{\rho \frac{\partial h}{\partial T} \bigg|_{\tilde{Q}}}{\rho \frac{\partial \rho'}{\partial p} \bigg|_{\tilde{Q}} \frac{\partial h}{\partial T} \bigg|_{\tilde{Q}} + \frac{\partial \rho}{\partial T} \bigg|_{\tilde{Q}} \left( 1 - \rho \frac{\partial h}{\partial p} \bigg|_{\tilde{Q}} \right)} \quad (32)$$

### Definition of Pseudo-Sound Speed

The definition of the pseudo-sound speed is selected to render the eigenvalues of the preconditioned system well conditioned. Examining equation [31], we note that this is readily achieved by choosing:

$$(c')^2 = \text{Min}(V^2, c^2) \quad (33)$$

where  $V$  is local convective velocity magnitude. This form corresponds to the standard inviscid choice of this parameter. From equation [32], we may thus express the preconditioning parameter in equation [30]:

$$\left. \frac{\partial \rho'}{\partial p} \right|_{\tilde{Q}} = \frac{1}{(c')^2} - \frac{\left. \frac{\partial \rho}{\partial T} \right|_{\tilde{Q}} \left( 1 - \rho \left. \frac{\partial h}{\partial p} \right|_{\tilde{Q}} \right)}{\rho \left. \frac{\partial h}{\partial T} \right|_{\tilde{Q}}} \quad (34)$$

### Numerical Method

The baseline numerical method is evolved from the UNCLE code of Taylor and his co-workers at Mississippi State University ([39], for example). UNCLE is based on a single-phase, pseudo-compressibility formulation. Roe-based flux difference splitting is utilized for convection term discretization. An implicit procedure is adopted with inviscid and viscous flux Jacobians approximated numerically. A block-symmetric Gauss-Seidel iteration is used to solve the approximate Newton system at each time-step.

The multi-phase extension of the code retains these underlying numerics but also incorporates two volume fraction transport equations, mass transfer, non-diagonal preconditioning, flux limiting, dual-time-stepping, and two-equation turbulence modeling. The fully compressible version incorporates an energy conservation equation.

### Discretization

The transformed system of governing equations is discretized using a cell centered finite volume procedure. Flux derivatives are computed as

$$\partial \hat{E} / \partial \xi = (\hat{E}_{i+1/2} - \hat{E}_{i-1/2}), \quad (35)$$

with similar expressions for  $\partial \hat{F} / \partial \eta$ ,  $\partial \hat{G} / \partial \zeta$ , and the corresponding viscous fluxes. The inviscid numerical fluxes are evaluated using a flux difference splitting procedure [45]:

$$\begin{aligned} \hat{E}_{i+1/2} = & \frac{1}{2} [E(Q_{i+1/2}^L) + \hat{E}(Q_{i+1/2}^R) + \\ & |\hat{A}|(Q_{i+1/2}^R, Q_{i+1/2}^L) \bullet (Q_{i+1/2}^R - Q_{i+1/2}^L)] \end{aligned} \quad (36)$$

where, with the non-diagonal preconditioner used here, the matrix dissipation operator is defined by  $|\hat{A}| = \Gamma(M|\Lambda|M^{-1})$ .

The extrapolated Riemann variables,  $Q_{i+1/2}^R$  and  $Q_{i+1/2}^L$  are obtained using a MUSCL procedure ([2], for example):

$$\begin{aligned} Q_{i+1/2}^R &= Q_{i+1} - \frac{\phi}{4} [(1-\kappa)(Q_{i+2} - Q_{i+1}) + (1+\kappa)(Q_{i+1} - Q_i)] \\ Q_{i+1/2}^L &= Q_i + \frac{\phi}{4} [(1-\kappa)(Q_i - Q_{i-1}) + (1+\kappa)(Q_{i+1} - Q_i)] \end{aligned} \quad (37)$$

For first order accuracy,  $\phi = 0$ . The choice  $\phi = 1$ ,  $\kappa = 1/3$ , yields the third order accurate upwind bias scheme used for the results presented in this paper.

The flows of interest here typically contain regions with sharp interfaces between liquid and gas phases. In addition, compressible flows admit shock waves and contact discontinuities. Accordingly, higher order discretization practices are required to retain adequate interface fidelity in the simulations. This is particularly important in three-dimensional super-cavitating vehicle or control surface computations such as those presented below. There, predicted lift and drag can be severely over-predicted if liquid phase (and its much higher inertia) diffuses numerically into low-lift gaseous regions of the lifting surface.

Attendant to the third order upwind bias scheme employed are overshoots in solution variables at these interfaces. These can be highly destabilizing, particularly for the volume fraction equations, if sufficient mass transfer or non-condensable vapor is present to yield  $\alpha_l \rightarrow 0$  locally. To ameliorate this difficulty, the flux evaluation is rendered locally first order in the presence of large gradients in  $\alpha_l$  or  $\alpha_{ng}$ . In solutions obtained for incompressible phasic constituents, this is affected through the use of a “dissipation sensor” in the spirit of Jameson et al. [14]. Specifically, a sensor is formulated for each coordinate direction as

$$v_i \equiv \frac{|\alpha_{i+1} - 2\alpha_i + \alpha_{i-1}|}{\alpha_{i+1} + 2\alpha_i + \alpha_{i-1}}. \quad (38)$$

This parameter is very small except in the immediate vicinity of liquid-gas interfaces. In this work, the higher order component of the numerical flux in equation [37], i.e. term  $\phi$ , is multiplied by  $(1-v_i)$ . In compressible solutions, shocks and contact discontinuities are admissible. Hence, it is necessary to limit interpolations based on the entire primitive vector. A standard form of the van Albada limiter [13] has been employed.

To illustrate the foregoing discretization issues, consider adjacent parallel streams of two constituents. In the absence of shear, if a flow-aligned Cartesian mesh is employed, the mixing layer interface will be perfectly preserved using the present modeling (no mass diffusion). This is true independent of the density ratio of the streams and whether first or higher order discretization is employed. However, if the interface encounters a region of significant grid non-orthogonality, the interface will be smeared.

We consider a two-dimensional grid slice extracted from the three-dimensional fin computation presented below, as illustrated in Figure 4a. Two-dimensional inviscid computations of a high density ratio mixing stream were computed on this grid. Gas and liquid ( $\rho_l/\rho_g = 1000$ ) were injected axially, at the same velocity, above and below an inlet location seen in Figure 4b. No solid boundaries are specified, so ideally, the interface would be perfectly preserved through the domain. However, the initially sharp mixing layer interface encounters severe grid non-orthogonality, as it does in full scale three-dimensional computations, even well away from solid boundaries, due to grid topology. Though this case is particularly pathological, regions where local grid quality suffers due to the geometry of the problem are inescapable in structured multiblock analyses of complex aerodynamic configurations.

Downstream of the grid “stripe” associated with the fin leading edge, Figures 4b and c show that the interface is badly smeared when first order discretization is employed ( $0.05 < \alpha_l < 0.95$  for 11-12 nodes). This is largely remedied when the 3rd order flux difference with dissipation sensor is employed ( $0.05 < \alpha_l < 0.95$  for 3-4 nodes).

The dissipation sensor used does not completely eliminate overshoots, as illustrated in Figure 4c. If the volume fractions are “clipped” at 1.0 after each pseudo-time-step the impact on the solution accuracy is minimal, as illustrated in Figure 4c. But, clipping causes the non-linear convergence to flat-line, so in general, we accept the modest overshoots in volume fraction.

Second order accurate backward differencing is used to discretize the physical transient term as

$$\Gamma_e \frac{\partial Q}{\partial t} \rightarrow \Gamma_e \frac{(3Q^{n+1,k} - 4Q^n + Q^{n-1})}{2\Delta t}, \quad (39)$$

where index n designates the physical time-step. Second order accurate central differencing is utilized for the viscous flux terms.

### Implicit Solution Procedure

Adopting Euler implicit differencing for the pseudo-transient term, equation [4] can be written in  $\Delta$ -form as

$$\left( \Gamma_e \left( \frac{3}{2\Delta t} \right) + \Gamma \left( \frac{1}{\Delta \tau} \right) + \frac{\partial}{\partial \xi_j} A_j - \frac{\partial}{\partial \xi_j} A_j^v - \hat{D} \right) \Delta \hat{Q} = - \Gamma_e \left( \frac{3Q^{n+1,k} - 4Q^n + Q^{n-1}}{2\Delta t} \right) - \frac{\partial}{\partial \xi_j} \hat{E}_j + \left( \frac{\partial}{\partial \xi_j} \right) \hat{E}_j^v + \hat{H} , \quad (40)$$

where  $\Delta \hat{Q} \equiv \hat{Q}^{n+1,k+1} - \hat{Q}^{n+1,k}$ , with index  $n$  designating the physical time-step and index  $k$  designating the pseudo-time-step. Terms  $A_j$ ,  $A_j^v$  and  $\hat{D}$  are the inviscid flux, viscous flux, and source Jacobians. The source Jacobian is evaluated analytically as illustrated below. The inviscid and viscous flux Jacobians are evaluated numerically as:

$$\begin{aligned} (A_j \Delta \hat{Q})_{i+1/2} &= \frac{\partial \hat{E}}{\partial \hat{Q}_L} \Delta \hat{Q}_L + \frac{\partial \hat{E}}{\partial \hat{Q}_R} \Delta \hat{Q}_R \approx \\ &\frac{\partial \hat{E}}{\partial \hat{Q}_L} \Delta \hat{Q}_i + \frac{\partial \hat{E}}{\partial \hat{Q}_R} \Delta \hat{Q}_{i+1} = \\ &\left[ \frac{\hat{E}(\hat{Q}_L + \epsilon, \hat{Q}_R) - \hat{E}(\hat{Q}_L, \hat{Q}_R)}{\epsilon} \right] \Delta \hat{Q}_i + \\ &\left[ \frac{\hat{E}(\hat{Q}_L, \hat{Q}_R + \epsilon) - \hat{E}(\hat{Q}_L, \hat{Q}_R)}{\epsilon} \right] \Delta \hat{Q}_{i+1} , \end{aligned} \quad (41)$$

where  $\epsilon$  is taken as the square root of a floating point number close to the smallest resolvable by the hardware.

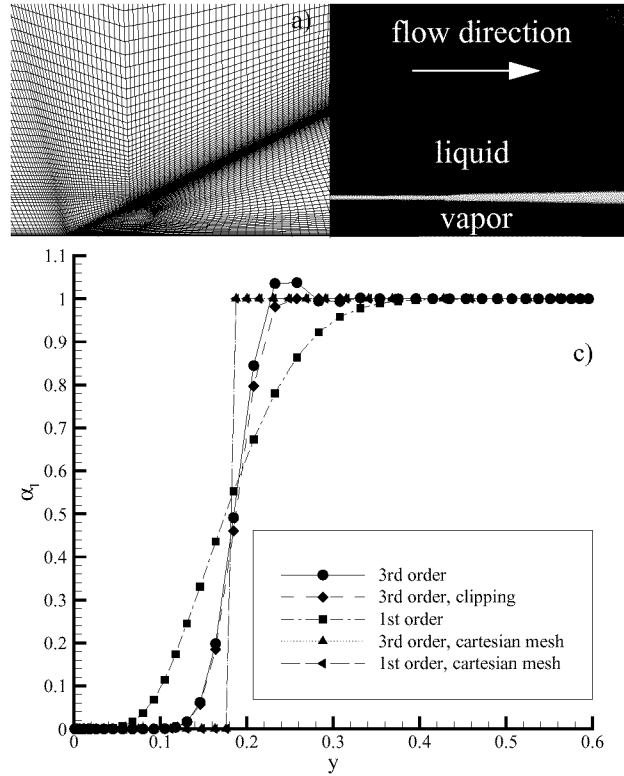


Figure 4. a) Two-dimensional grid slice extracted from three-dimensional control fin model. b) Predicted liquid volume fraction contours using present third order discretization. c) Predicted liquid volume fraction profiles for various grids and discretizations.



The pseudo-time-step is defined based on the spectral radii of  $\Gamma^{-1}A_j$  as

$$\Delta\tau = \frac{\text{CFL}}{\sum_j |U_j + C_j|}. \quad (42)$$

For steady state computations, the physical time-step,  $\Delta t$ , is set to infinity, and a CFL number of 3-5 is typically used.

In the present work, we seek to resolve transient features characterized by the quasi-periodic shedding of vorticity and gas from the cavity. Strouhal numbers on the order of 0.1 are encountered in practice. Accordingly, non-dimensional physical time-steps on the order of .005 - .01 are required. A CFL number of 3-5 is typically used for the inner iterates in transient computations. As illustrated below, this gives rise to a dual-time scheme that provides a 1 to 3 order-of-magnitude drop in residuals in 5-10 pseudo-time-steps.

Optimum non-linear convergence is obtained using a pseudo-compressibility parameter,  $\beta^2/U_\infty^2 \cong 10$ .

Upon application of the discretization and numerical linearization strategies defined, equation [40] represents an algebraic system of equations for  $\Delta Q$ . This block (6x6 blocks) septadiagonal system is solved iteratively using a block symmetric Gauss-Seidel method. Five sweeps of the BSGS scheme are applied at each pseudo-time-step.

### Source Terms

Following the strategy of Venkateswaran et al. [40] for the numerical treatment of mass transfer source terms in reacting flow computations, we identify a source and sink component of the mass transfer model and treat the sink term implicitly and the source term explicitly. Specifically, with reference to equation [1] we have

$$H^{+/-} = \left[ \dot{m}^{+/-} \left( \frac{1}{\rho_l} - \frac{1}{\rho_v} \right), 0, 0, 0, \dot{m}^{+/-} \left( \frac{1}{\rho_l} \right), 0 \right]^T. \quad (43)$$

With  $\dot{m}^-$  from equation [14] we have

$$\Delta H^- \equiv D^- \Delta Q, \text{ with } D^- \equiv \partial H^- / \partial Q. \quad (44)$$

It can easily be shown that the non-zero eigenvalue of  $D^-$  is

$$\lambda(D^-) = C_{\text{dest}} \rho_v \left[ \left( \frac{1}{\rho_l} - \frac{1}{\rho_v} \right) \alpha_l + \left( \frac{1}{\rho_l} \right) (p - p_v) \right] \quad (45)$$

which is less than zero for  $\rho_v < \rho_l$ . Hence, the identification of  $\dot{m}^-$  as a sink is numerically valid. Implicit treatment of this term provides that  $\alpha_l$  approaches zero exponentially, so that cases like those considered below, where significant mass transfer results in extremely low liquid volume fractions, remain stable.

The production mass transfer term is treated explicitly. A relaxation factor of 0.1 is applied at each pseudo-time-step to keep this term from destabilizing the code in early iterations.

### Turbulence Model Implementation

The turbulence transport equations are solved subsequent to the mean flow equations at each pseudo-time-step. A first order accurate flux difference splitting procedure similar to that outlined above for the mean flow equations is utilized for convection term discretization. The  $k$  and  $\epsilon$  equations are solved implicitly using conventional implicit source term treatments and a 2x2 block symmetric Gauss-Seidel procedure.

## Boundary Conditions

Velocity components, volume fractions, turbulence intensity, and turbulence length scale are specified at inflow boundaries and extrapolated at outflow boundaries. Pressure distribution is specified at outflow boundaries ( $p=0$  for single-phase or non-buoyant multi-phase computations) and extrapolated at inflow boundaries. At walls, pressure and volume fractions are extrapolated, and velocity components and turbulence quantities are enforced using conventional wall functions. Boundary conditions are imposed in a purely explicit fashion by loading “dummy” cells with appropriate values at each pseudo-time-step.

## Parallel Implementation

The multiblock code is instrumented with MPI for parallel execution based on domain decomposition. Inter-block communication is affected at the non-linear level through boundary condition updates and at the linear solver level by loading  $\Delta Q$  from adjacent blocks into “dummy” cells at each SGS sweep. This is not as implicit as solving an optimally ordered linear system for the entire domain at each SGS sweep, but, as demonstrated below, this potential shortcoming will not deteriorate the non-linear performance of the scheme if the linear solver residuals are reduced adequately at each pseudo-time-step. The authors routinely employ 48-80 processors for three-dimensional, unsteady analyses.

## Results

Three sets of results from the authors’ recent research are presented. The first set includes axisymmetric steady-state and transient analyses of natural and ventilated cavitation about several configurations. These solutions are compared to experimental measurements to demonstrate the capability of the modeling employed. The second set of results includes a variety three-dimensional analyses of sheet- and supercavitating flows of relevance to high speed vehicles and turbomachinery. The third set of results includes compressible simulations of a vehicle propulsion plume and a high speed supercavitating projectile.

### Axisymmetric Analyses

#### Steady State and Transient Natural and Ventilating Cavitation about a Series of Axisymmetric Forebodies

Due to the authors’ principal research interests in supercavitating vehicles, an emphasis of our CFD development and validation efforts has been on axisymmetric bodies. In this regard, we have used data due to Rouse and McNown [29] as well as that due to Stinebring et al. [36], [37] for validation purposes.

Rouse and McNown [29] carried out a series of experiments wherein cavitation induced by convex curvature aft of various axisymmetric forebodies with cylindrical afterbodies was investigated. At low cavitation numbers, these flows exhibit natural cavitation initiating near or just aft of the intersection between the forebody, or *cavitator*, and the cylindrical body. For each configuration, measurements were made across a range of cavitation numbers, including a single phase case (large  $\sigma$ ). Surface static pressure measurements were taken along the cavitator and after-body. Photographs were also taken from which approximate bubble size and shape were deduced.

Several of the Rouse-McNown configurations were analyzed. These included 0-caliber (blunt), 1/4-caliber, 1/2-caliber (hemispherical), 1-caliber, and 2-caliber ogives and conical ( $22.5^\circ$  cone half-angle) cavitator shapes. The experiments were performed at Reynolds numbers greater than 100,000 based on maximum cavitator (i.e., after-body) diameter. A value of  $Re = 136000$  was used for the simulations. In order to properly assess grid resolution requirements, a range of grid sizes was used. For the hemispherical and conical configurations, grid sizes of  $65 \times 17$ ,  $129 \times 33$  and  $257 \times 65$  were run. Figure 5 demonstrates that differences between predicted surface pressures for the medium and fine meshes are small. The fine meshes were used for all subsequent calculations presented here. For the blunt fore-body, a two-block grid topology had to be used, and a

mesh consistent with the resolution and clustering of the other head-forms was utilized (65x49, 257x65 for blocks 1 and 2; see Figure 9b).

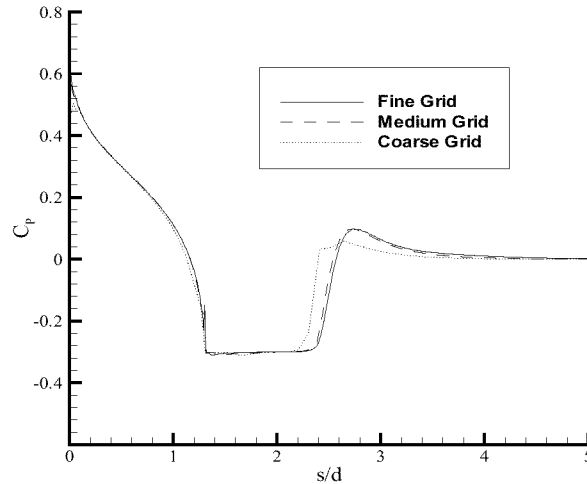


Figure 5. Comparison of predicted surface pressure distributions for naturally cavitating axisymmetric flow over a conical cavitator-cylindrical after-body configuration,  $\sigma = 0.3$ . Coarse (65x17), medium (129x33) and fine (257x65) mesh solutions are plotted.

Figures 6 through 24 show sample results for these axisymmetric computations. Figure 6a shows predicted and measured surface pressure distributions at several cavitation numbers for the 1-caliber ogive forebody with cylindrical afterbody. As the cavitation number is decreased from near a critical “inception” value, a cavitation bubble forms and grows. The presence of the bubble manifests itself as a decrease in magnitude, flattening and lengthening of the pressure minimum along the surface. Also, bubble closure gives rise to an overshoot in pressure recovery due to the local stagnation associated with free-stream liquid flowing over the convex curvature at the aft end of the bubble. The code is seen to accurately capture these physics as evidenced by the close correspondence between predicted and measured pressure distributions. Figure 6b illustrates the qualitative physics as captured by the model. There, surface pressure contours, field liquid volume fraction contours, selected streamlines and the grid used are shown for the 1-caliber case at  $\sigma = 0.15$ . For this case, the cavitation bubble is quite long ( $L/d > 3$ ). As with all large cavitation bubbles, the closure region is characterized by an unsteady “re-entrant” jet. The significant flow recirculation and associated shedding of vorticity and vapor in these flows require that a transient simulation be carried out. This is discussed further below. The solution depicted in Figure 6b represents a snapshot in time of an unsteady simulation.

Figures 7-9 provide similar comparisons for hemispherical, conical and blunt ogives. Specifically, Figures 7a, 8a and 9a show comparisons between predicted and measured surface pressure distributions for these three configurations at a range of cavitation numbers. In Figures 7b, 8b and 9b, surface pressure contours, field liquid volume fraction contours, selected streamlines and the grid are illustrated for selected cavitation numbers. In each case, a discrete bubble shape is observed, but the aft end of the predicted bubble does not exhibit a smooth “ellipsoidal” closure. Indeed, due to local flow reversal (reentrant jet), liquid is swept back underneath the vapor pocket. The pressure in this region retains the nearly constant free stream liquid flow value impressed through the bubble. Similar closure region observations have been made by Chen and Heister [6] and others.

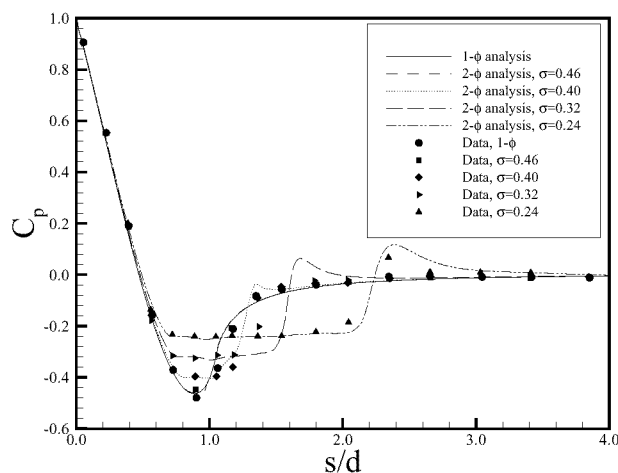


Figure 6a. Comparison of predicted and measured surface pressure distributions at several cavitation numbers for a 1-caliber ogive forebody.

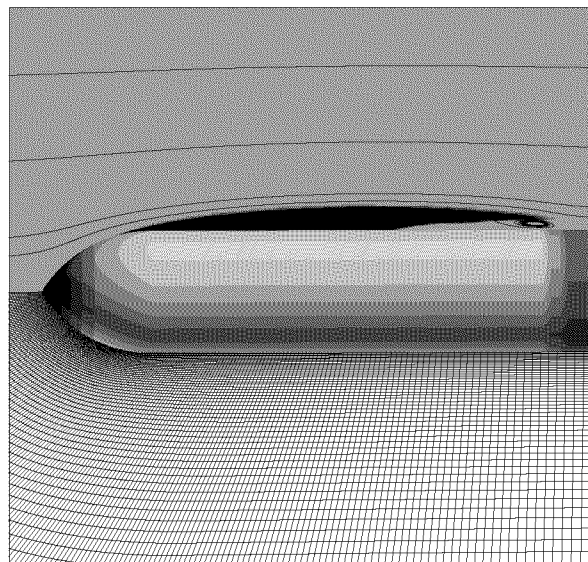


Figure 6b. Predicted liquid volume fraction and surface pressure contours, selected streamlines and computational grid for a 1-caliber ogive forebody,

As with the 1-caliber ogive, the predicted pressure distribution for the hemispherical cavitator is very well predicted, but Figure 8b illustrates that the simulations underpredict the length of the bubble for the  $22.5^\circ$  half-angle conical head form at all cavitation numbers, though qualitative trends remain correctly predicted. Although fairly good quantitative agreement is obtained for the blunt fore-body at low cavitation numbers, shortcomings of the present modeling are evident. First, even the single phase pressure distribution shows significant discrepancy from the data. In particular, the characteristic flattening of the measured pressure distribution due to a large recirculation zone aft of the corner is significantly underpredicted. Such a “forward facing step” flow is well known to provide significant challenges to single phase turbulence models. The conventional model employed here (high Reynolds number  $k-\epsilon$ ) has well-documented difficulties with stagnated, high strain and recirculating flows. All of these characteristics are embodied in the blunt head-form flow. Our efforts to “remedy” these single phase turbulence modeling shortcomings by deploying several approaches that have appeared in the literature ( $q-\omega$ , sublayer modeling, RNG) have yet to yield a fully satisfactory resolution. As observed by Shyy [33], [“there are no quick, practical solutions to handle this challenge. However, models capable of handling (i) substantial departure from equilibrium between production and dissipation of the turbulent kinetic energy, (ii) anisotropy between main Reynolds stress components, and (iii) turbulence-enhanced mass transfer across the phase inter-face, should be emphasized”].

Several parameters of relevance in the characterization of cavitation bubbles include body diameter,  $d$ , bubble length,  $L$ , bubble diameter,  $d_m$ , and form drag coefficient associated with the cavitator,  $C_D$ . Some ambiguity is inherent in both the experimental and computational definition of the latter three of these parameters. Bubble closure location is difficult to define due to unsteadiness and its dependence on after-body diameter (which can range from 0 [isolated cavitator] to the cavitator diameter). Accordingly, bubble length is often, and here, taken as twice the distance from cavity leading edge to the location of maximum bubble diameter (see Figure 10). The form drag coefficient is taken as the pressure drag on an isolated cavitator shape. For cavitators with afterbodies, such as here, the pressure contribution to  $C_D$  associated with the back of the cavitator is assumed equal to the cavity pressure ( $\approx p_v$ ). For the simulations,  $d_m$  is determined by examining the  $\alpha_l = 0.5$  contour and determining its maximum radial location.

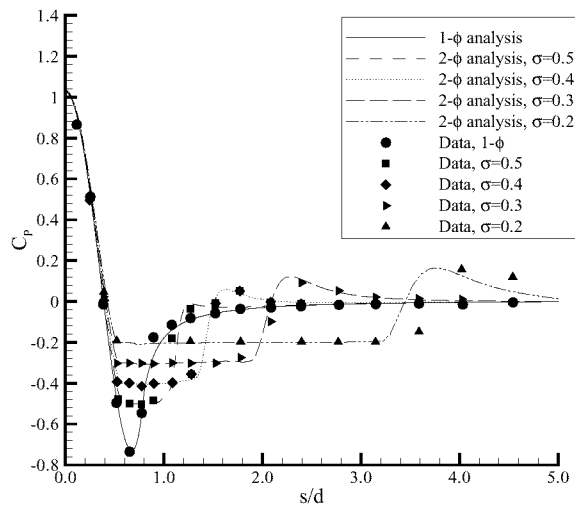


Figure 7a. Comparison of predicted and measured surface pressure distributions at several cavitation numbers for a hemispherical fore-body.

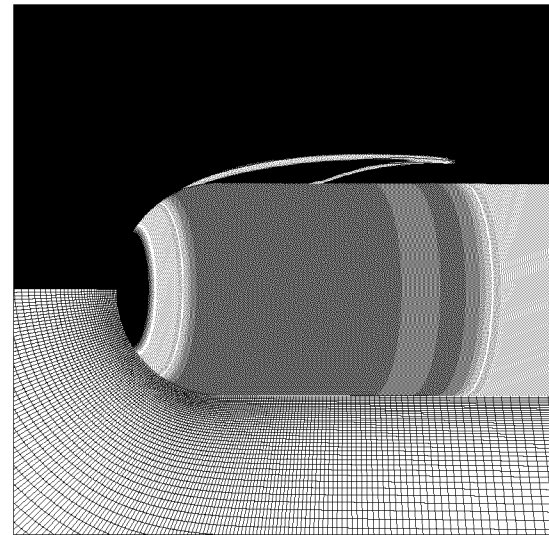


Figure 7b. Predicted liquid volume fraction and surface pressure contours, selected streamlines and computational grid for a hemispherical fore-body,  $\sigma=0.3$ .

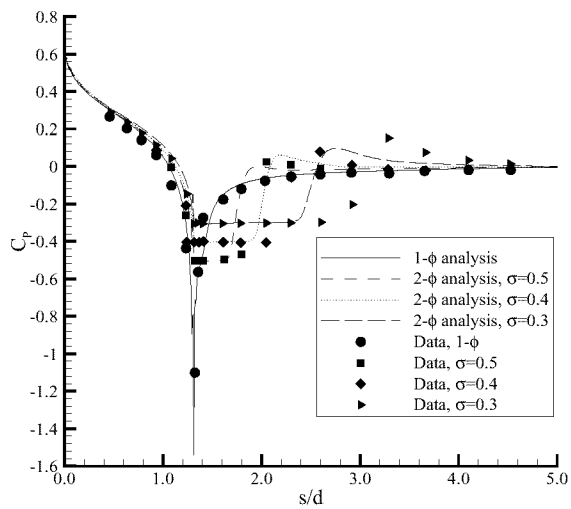


Figure 8a. Comparison of predicted and measured surface pressure distributions at several cavitation numbers for a conical fore-body.

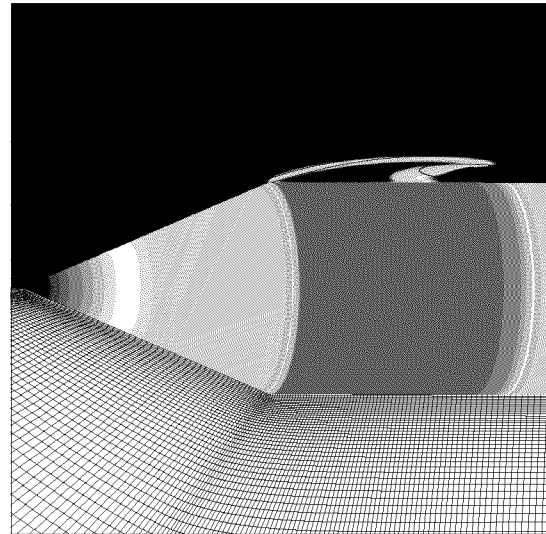


Figure 8b. Predicted liquid volume fraction and surface pressure contours, selected streamlines and computational grid for a conical fore-body,  $\sigma=0.3$ .

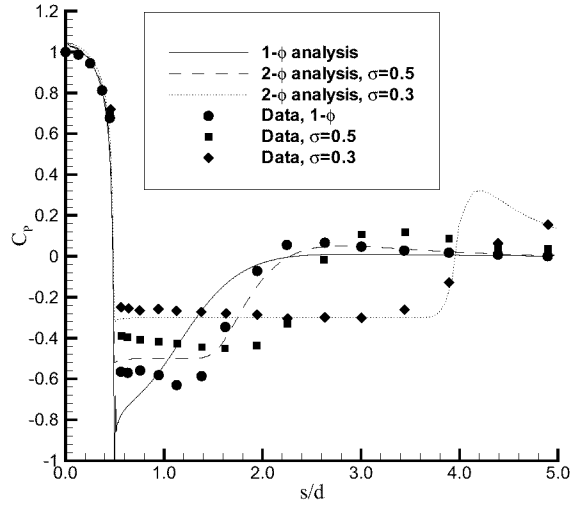


Figure 9a. Comparison of predicted and measured surface pressure distributions at several cavitation numbers for a blunt fore-body.

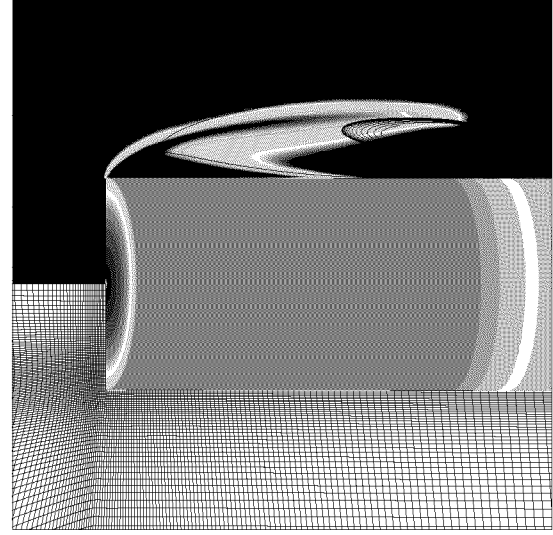


Figure 9b. Predicted liquid volume fraction and surface pressure contours, selected streamlines and computational grid for a blunt fore-body,  $\sigma=0.4$ .

In Figure 11a, the quantity  $L/(dC_D^{1/2})$  is plotted against cavitation number for a large number of experimental data sets assembled by May [22] from a variety of sources and for numerous simulations made with six cavitator shapes. That  $L/(dC_D^{1/2})$  should correlate with  $\sigma$  has been long established theoretically and experimentally (Reichardt [27], Garabedian [11], for example). Despite the significant uncertainties associated with experimental and computational evaluation of  $L$  and  $C_D$ , the data and simulations do correlate well, close to independently of cavitator shape. The cone shaped cavitator exhibits some underprediction of this parameter at higher cavitation numbers, consistent with the bubble length underprediction observed in the pressure distribution comparisons presented above.

The so-called *fineness ratio* of the cavity,  $L/d_m$ , is plotted against cavitation number in Figure 11b for the same experimental and computational data sets. These parameters again correlate well for both experiment and simulation, though at higher cavitation numbers there is a spread in both. Considering the difficulties in quantifying smaller bubble sizes, we hesitate to draw any conclusions as to the possible sources of this spread.

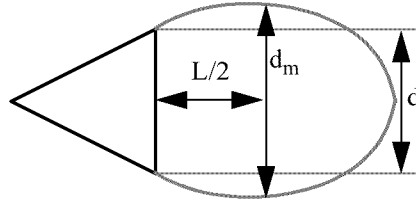


Figure 10. Bubble length and bubble diameter definitions.

In the cases considered so far, steady-state solutions were obtained for higher cavitation numbers. At lower cavitation numbers (i.e. larger bubbles), significant large scale unsteadiness appears in the aft region of the bubble/reentrant jet region. Vorticity and condensable vapor are shed from this region. Accordingly, transient simulations (dual-time stepping) were performed when pseudo-timestepping failed to converge. For the 0-, 1/4-, 1/2-, 1- and 2-caliber and conical cavitator shapes, transient computations were performed for cavitation numbers less than or equal to  $\sigma = 0.5, 0.3, 0.35, 0.15, 0.05$  and  $0.4$ , respectively. Non-dimensional physical time steps of  $\Delta t/t_\infty = 0.007$  were utilized for these computations. In Figures 11a and 11b, time accurate CFD results are represented with filled symbols, steady state results with open symbols.

## Ventilated Cavitation

Ventilated cavities are also of interest to the authors because for large enough values of free stream pressure the only way to generate large cavities is to inject some mixture of condensable and non-condensable gases into the flow near the body leading edge. In general, ventilated cavities exhibit similar dynamics to natural cavities (May [22]). Ventilated cavities do, however, tend to be more stable than natural cavities near the aft end of the cavitation bubble. Also, as discussed in the authors' companion paper [38] all non-condensable gas must mix with the free stream liquid and be transported downstream.

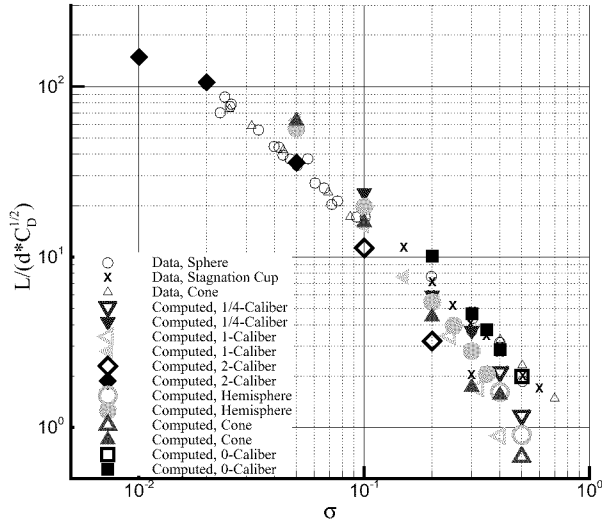


Figure 11a. Comparison of  $L/(dC_D^{1/2})$  vs.  $\sigma$  for numerous fore-body shapes. Experimental data adapted from May [22]. Open symbols represent steady computations, filled symbols represent transient computations.

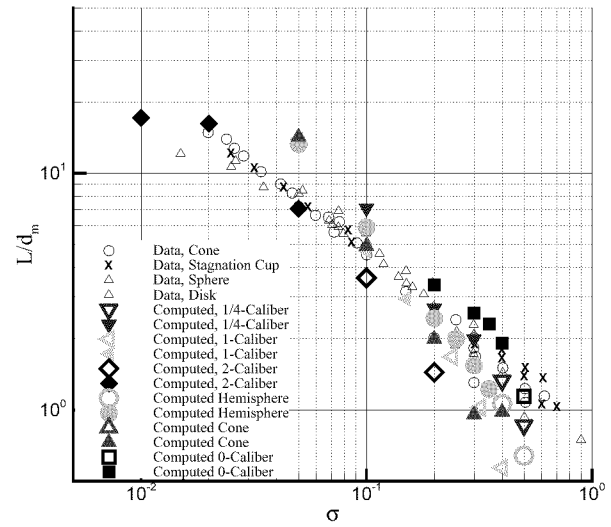


Figure 11b. Comparison of  $L/d_m$  vs.  $\sigma$  for numerous fore-body shapes. Experimental data adapted from May [22]. Open symbols represent steady computations, filled symbols represent transient computations.

The axisymmetric blunt fore-body configuration presented above was run with no mass transfer but with non-condensable gas injection just aft of the leading edge. A range of injection mass flow rates were specified, yielding a range of ventilated cavity sizes. The resulting cavities do not close in the sense that all vapor is condensed, however a distinct bubble shape is observed whose geometry is quantified as detailed above. This is illustrated in Figure 12, where the predicted liquid volume fraction fields are shown for the blunt head-form natural and vented cavities at  $\sigma = 0.4$ . (The cavitation number in ventilated cavities is defined not from the vapor pressure but from the cavity pressure.)

In Figures 13a and 13b,  $L/(dC_D^{1/2})$  and  $L/d_m$  are plotted for the blunt head-form at a range of cavitation numbers. The natural cavity results presented above are reproduced in these plots along with the results of six ventilated cavity runs. (Note that the cavitation number is not explicitly specified in the ventilated case; rather it is an outcome of specified ventilation flow rate. This is why the ventilated data predictions in Figures 13a and 13b are not at precisely the same cavitations numbers as the natural ventilation cases.) The similarity between the natural and ventilated cavity results are generally affirmed by the simulations, in that these parameters cor-

relate well with each other and with the experimental data provided in Figures 11a and 11b.

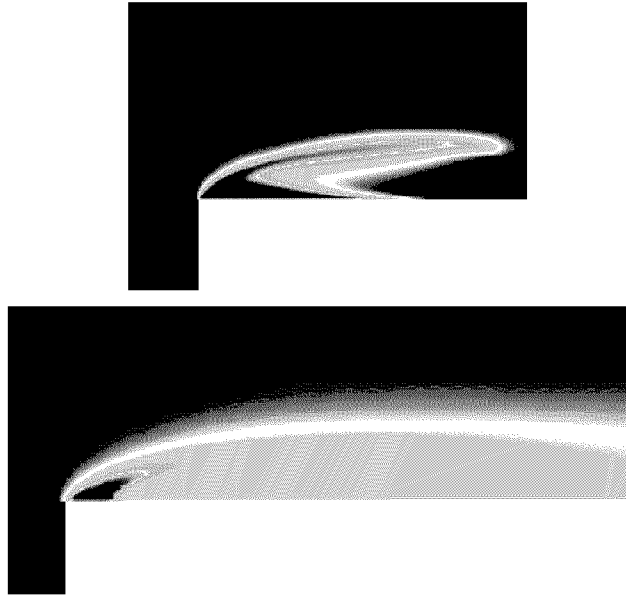


Figure 12. Predicted liquid volume fraction contours for axisymmetric natural and ventilated cavities about a cylindrical configuration with blunt fore-body ( $\sigma = 0.4$ ).

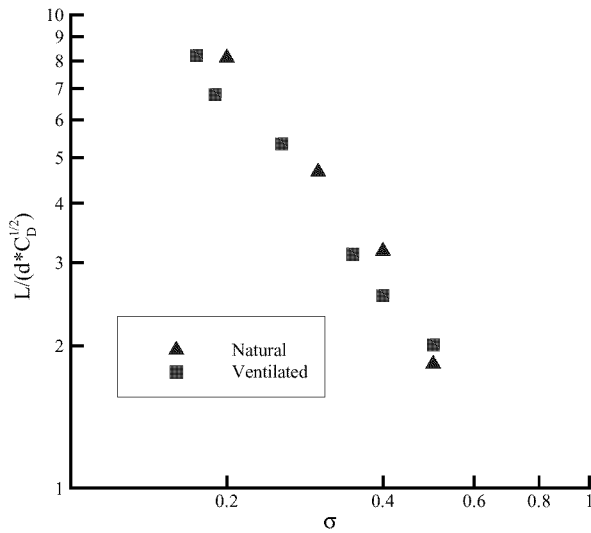


Figure 13a. Comparison of  $L/(d \cdot C_D^{1/2})$  vs.  $\sigma$  for natural and ventilated cavities about a blunt fore-body.

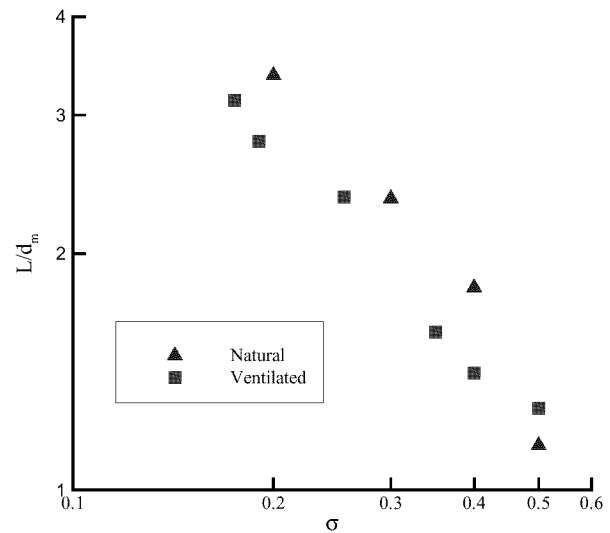


Figure 13b. Comparison of  $L/d_m$  vs.  $\sigma$  for natural and ventilated cavities about a blunt fore-body.

### Unsteady Characteristics of Cavities

As mentioned above, developed cavities exhibit large scale unsteadiness associated with re-entrant jets, periodic ejection of non-condensable gas, and cavity “pulsations”. Accordingly, we have employed a time-accurate formulation in the analysis of developed cavitation. Our particular interest in cavitator design has motivated the hydrodynamic performance parameter model assessments and validation carried out above. There, most of the simulations were unsteady and the presented results were time averaged.

There is also particular interest in the time dependent (as opposed to time averaged) characteristics of devel-



oped cavities, as these physics play importantly in vehicle acoustics, body wetting and bubble cloud collapse. Motivated by the former two, we have carried out an assessment of the accuracy of the predicted temporal statistics provided by the code.

We first illustrate the qualitative temporal characteristics of an analysis of a bluff forebody shape at moderate cavitation numbers. In such flows it is well known that the entire cavity can be highly unsteady, with “re-entrant” liquid issuing quasi-periodically from the aft end of the bubble and traveling all the way to the front of the bubble. In Figure 14, a time-sequence of predicted vapor volume fraction is reproduced for a 1/4-caliber ogive simulation at a Reynolds number of  $1.36 \times 10^5$  and a cavitation number of 0.3. A  $193 \times 65$  mesh and a non-dimensional physical time-step of 0.007 was used for this computation. Clearly captured is the transport of a region of liquid towards the front of the cavity. There, the liquid interacts with the bubble leading edge, the top of this liquid region being sheared aftward while the bulk of the fluid proceeds upstream “pinching off” the bubble near the leading edge.

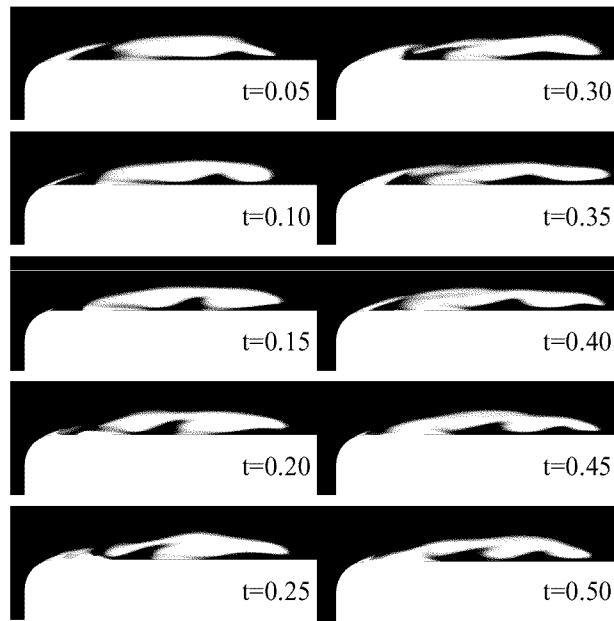


Figure 14. Time sequence of predicted vapor volume fraction for flow over a 1/4 caliber ogive with cylindrical afterbody,  $\sigma = 0.3$

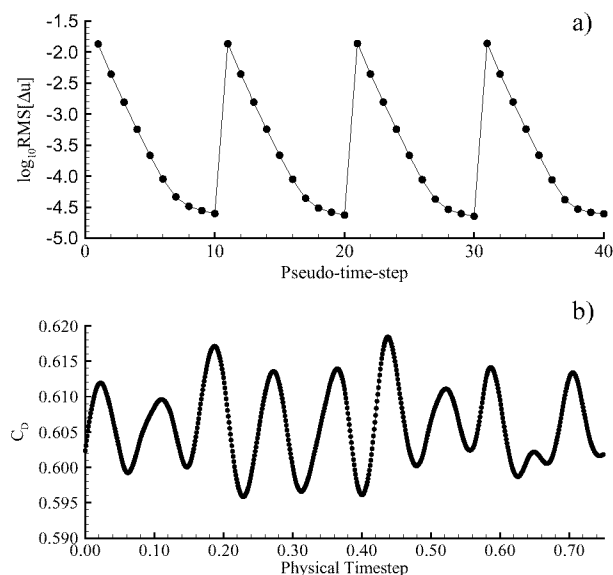


Figure 15. a) Pseudo-time convergence history at four successive physical time steps for transient flow over a 1/4 caliber ogive with cylindrical afterbody,  $\sigma = 0.3$ . b) Segment of time history of predicted  $C_D$  for this case.

Figure 15 shows two other elements of this particular transient simulation. The inner- or pseudo-time convergence history for four successive physical time steps is shown in Figure 15a. Nearly a three order-of-magnitude drop in the axial velocity residuals is obtained at each physical time step using 10 pseudo-time-steps. Figure 15b shows a segment of the time history of predicted drag coefficient for this case

Stinebring et al. [36] documented the unsteady cycling behavior of several axisymmetric cavitators. Their report included results for both ventilated and natural cavitation. The unsteady performance of  $45^\circ$  ( $22.5^\circ$  half-angle) conical, hemispherical, and 0-caliber ogival cavitators at a range of cavitation numbers were documented. Natural cavitation analysis comparisons have been included here.

Figure 16 contains a series of snapshots of the predicted volume fraction field from an unsteady model computation of flow over a 0-caliber (blunt) cavitator. Here the Reynolds number (based on diameter) was  $1.46 \times 10^5$  and the cavitation number was 0.3. This result is presented over an approximate model cycle. The figure also includes the corresponding time segment of drag coefficient. Note that the spikes in drag near  $t=37.725$  and  $t=38.925$  seconds correspond to reductions in the relative amount of vapor near the sharp leading edge. This marks the progress of a bulk volume of liquid from the closure region to the forward end of the cavity as part of the reentrant jet process. Although far from regular, these spikes also delineate the approximate model cycle.

The computed physics in Figures 14 and 23 correspond qualitatively to film footage of blunt cavitators at intermediate cavitation numbers. This is illustrated in Figure 17 which is a photograph (adapted from Stinebring [37]) of a 0-caliber axisymmetric cavitator operating at  $Re_D = 2.9 \times 10^5$ ,  $\sigma \approx 0.35$ . This picture serves to illustrate the basic phenomenon of natural sheet cavitation as it is captured by the model. This result is notable for the spatially and temporally irregular nature of the computed flow field. Even after significant integration effort, a clearly periodic result had not emerged. Thus, to deduce the dominant frequency with some confidence, it was necessary to apply ensemble averaging.

Note, in Figure 16 that over a significant portion of the sequence, the leading, or formative, edge of the cavity sits slightly downstream from and not attached to the sharp corner. In their experiments, Rouse and McNown observed this phenomenon. They suggested that this delay in cavity formation was due to the tight separation

eddy which forms immediately downstream of the corner and, hence, locally increases the pressure. The corresponding evolution of cavitation further downstream, at the separation interface, was proposed to be due to tiny vortices. These vortices, after some time, subsequently initiate the cavity.

Figure 18 shows a single frame at  $t=37.8$  seconds from the same model calculation (as shown in Figure 23). Here, to clarify what is captured, the volume fraction contours have been enhanced with illustrative streamlines. Note that these are streamlines drawn from a frozen time slice. Nonetheless, if all of the details envisioned by Rouse and McNown were present, the streamlines should indicate smaller/tighter vortical flows. The current level of modeling was unable to capture small vortical structures in the flow. However, the overall computation was apparently able to capture the gross affects of these phenomena and reproduce a delayed cavity. In fact from examination of the cavity cycle evolution shown in Figure 23, and the streamlines shown in the snapshot, it appears that gross unsteadiness is driven by a combination of a reentrant jet and some type of cavity pinching. The pinching process is particularly well demonstrated in Figure 23 from  $t=38.125$  to  $38.325$  seconds. However, rather than complete division and convection into the free stream, it should be noted that, in later frames of Figure 23, the pinched portion of the cavity appears to rejoin the main cavity region.

The low frequency mode apparent in most of the experimental 0-caliber results appears to have been captured at the lowest cavitation number ( $\sigma=0.3$ ), as shown in Figure 23, and is evidenced in the test photograph (Figure 17). In Figure 19, the drag coefficient history for a 40 model second interval from the same computation as in Figure 23 is shown. Here, a clear picture of the persistence, over a long integration time, of the irregular flow behavior is documented. At higher cavitation numbers, the current set of 0-caliber cavitation results indicate a more regular periodic motion. This is contrary to the experimental data. However, as Figure 18 indicates, the ability to capture this motion at any cavitation number may not necessarily require the explicit capture of the finer flow details of the vortical flow structure. This is encouraging and suggests that with increased computational effort, without altering the current physical model, the representation of this phenomenon could be improved over a greater range of cavitation numbers.

Figure 20 presents the spectral content of the result given in Figure 19. This power spectral density plot is based on four averaged Hanning windowed data blocks of the time domain result. To eliminate the start-up transient effect, the record was truncated, starting at  $t=10$  seconds and, to tighten the resulting confidence intervals, more time domain results, after  $t=40$  seconds were included. As is typical of highly nonlinear sequences, the experience of this unsteady time integration demonstrated that, additional time records merely enrich the power spectral density function. However, the additional records do serve to improve the confidence intervals, and, therefore, add reliability to the numerical convergence process. The model result used was, as indicated by the confidence intervals, sufficient for a comparison to experimental, unsteady results.

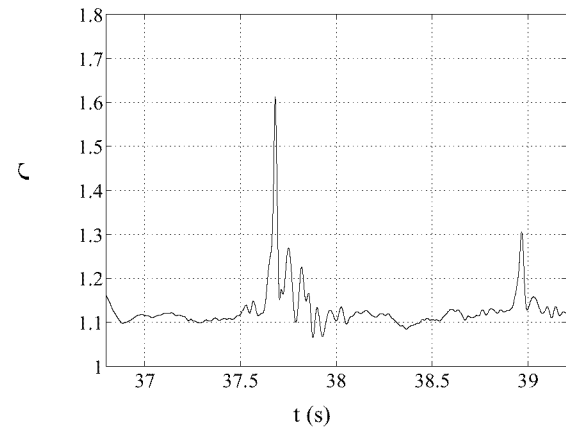
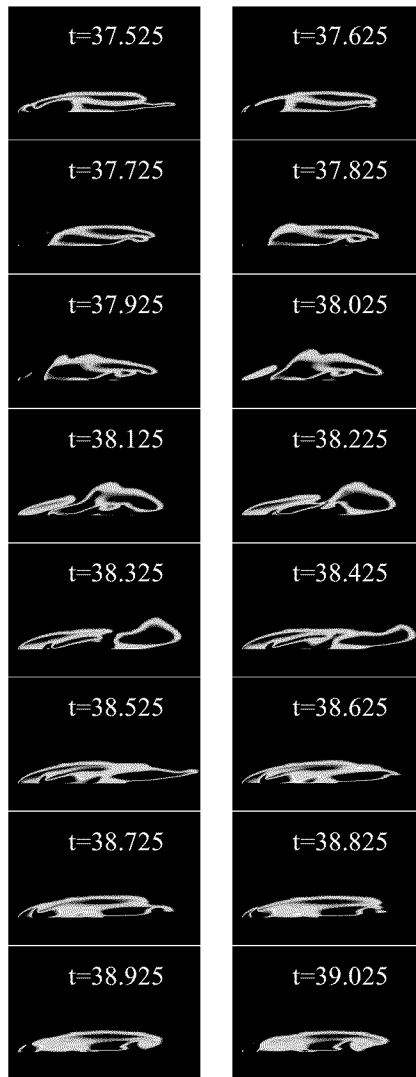


Figure 16. Modeled flow over a 0-caliber ogive. Liquid volume fraction contours and corresponding drag history.  $\sigma=0.3$ .  $Re_D=1.46 \times 10^5$ .



Figure 17. Zero caliber ogive in water tunnel at  $Re_D=2.9 \times 10^5$ ,  $\sigma \approx 0.35$  (adapted from Stinebring [37]).

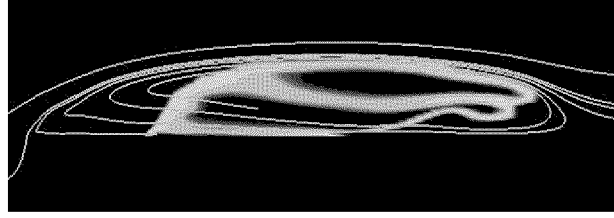


Figure 18. Snapshot of modeled flow over a 0-caliber ogive. Liquid volume fraction contours and selected streamlines.  $\sigma=0.3$ .  $Re_D=1.46 \times 10^5$ .

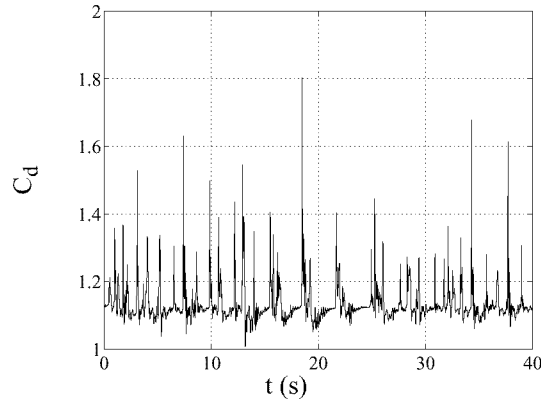


Figure 19. Model time record of drag coefficient for flow over a 0-caliber ogive at  $Re_D=1.46 \times 10^5$  and  $\sigma=0.3$ . In model units,  $D/U_\infty = 0.146$  (s), physical time step,  $\Delta t = 0.001$  (s).

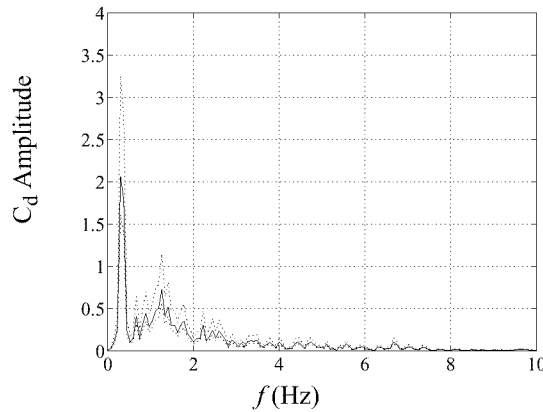


Figure 20. Results for 0-caliber ogive at  $Re_D=1.46 \times 10^5$  and  $\sigma=0.3$ . Power spectral density function with 50% confidence intervals shown.

Figure 21 contains a series of snapshots from the unsteady model computation of a hemispherical cavitator at a Reynolds number (based on diameter) of  $1.36 \times 10^5$  and a cavitation number of 0.2. This result is presented over a period slightly longer than the approximate model cycle. In this case the model Strouhal frequency is 0.0326. There are ten frames presented, and the first (or last) nine of those ten constitute an approximate model cycle. The drag history trace in Figure 22 demonstrates how, relative to the modeled flow over the blunt forebody, the pattern of flow over the hemispherical forebody is regular and periodic. This is consistent with experimental observations made (for example) by Rouse and McNown [29]. Note the evolution of flow shown in Figure 21 as it compares to the drag history shown in Figure 22. As would be expected, the large

spike in drag corresponds to the minimum in vapor shown near the modeled  $t=1.6$  seconds.

Figure 23 contains a time record of drag coefficient during modeled flow over a conical forebody and cylinder at a Reynolds number of  $1.36 \times 10^5$  and cavitation number of 0.2. The Strouhal frequency based on this result is 0.0383. As anticipated, due to the expected stability of cavities about this shape, this model flow exhibited very regular cycling with little additional strong components from secondary modes.

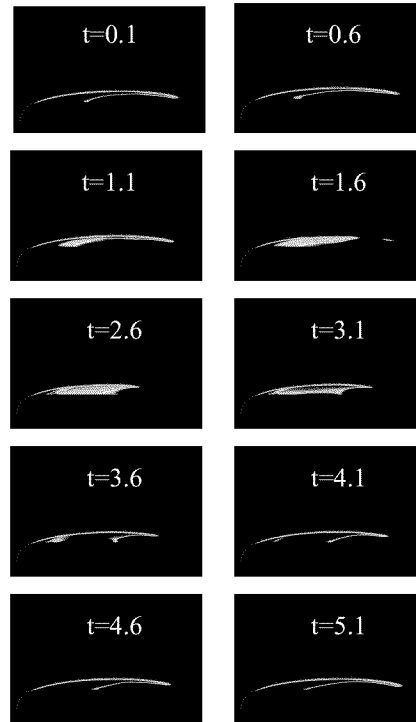


Figure 21. Liquid volume fraction countours. Modeled flow over a hemispherical forebody and cylinder.  $\sigma=0.2$ ,  $Re_D=1.36 \times 10^5$ .

Figure 24 contains a large survey of unsteady computational and experimentally obtained data [36]. The numerical results in this figure summarize this validation effort. Here, Strouhal frequency is shown over a range of cavitation numbers. Computational results are given for hemispherical, 1/4-caliber, conical, and 0-caliber forebodies. Unsteady experimental data is included for the hemispherical, conical and 0-caliber shapes. Computational results for the hemisphere, 1/4-caliber and conical forebodies, were obtained at a Reynolds number based on diameter of  $1.36 \times 10^5$ . For the 0-caliber ogive, computations were made at a Reynolds number of  $1.46 \times 10^5$ . In addition, for the hemisphere, results are included for Reynolds numbers of  $1.36 \times 10^6$  and  $1.36 \times 10^7$ . The experimental results included in the figure were obtained at Reynolds numbers ranging from  $3.5 \times 10^5$  to  $1.55 \times 10^6$ .

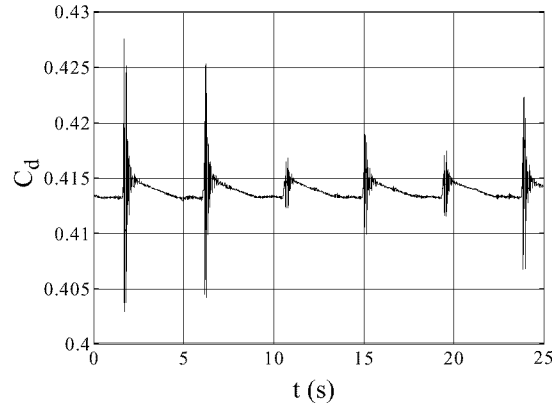


Figure 22. Unsteady drag coefficient. Flow over a hemispherical forebody and cylinder.  $\sigma=0.2$ ,  $Re_D=1.36 \times 10^5$ . In model units,  $D/U_\infty = 0.136$  (s), physical time step,  $\Delta t = 0.001$  (s).

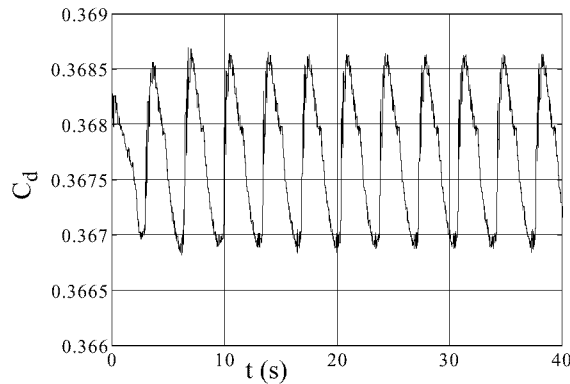


Figure 23. Predicted time record of drag coefficient for flow over a conical forebody and cylinder at  $Re_D=1.36 \times 10^5$  and  $\sigma=0.3$ . In model units,  $D/U_\infty = 0.136$  (s), physical time step,  $\Delta t = 0.0025$

As a blanket observation, the spread of data between the experiments and computations in Figure 24 is significant. However, there are several encouraging items to be reviewed. It is clear that (for a given cavitation number) the computational results are bounded by the experimental data, and the proper trends (rate of change of Strouhal frequency with cavitation number) are well captured. More insight into the physical relevance of the data requires examination of specific results.

For the hemispherical forebody results, as may be seen in Figure 24, there is a significant but almost constant offset between the measured unsteady data and the modeled results both of which appear to follow a linear trend over the range presented. An interesting result occurs in the model data for the hemispherical forebody with a Reynolds number of  $1.36 \times 10^7$  (pentagrams in Figure 24). Here the numerical results appear to agree quite well with the experimental data for hemispherical forebodies. The experiments were taken at an order of magnitude lower Reynolds number, but the agreement is apparent in both cases where model results have been obtained. For design purposes, this may suggest an avenue towards model calibration.

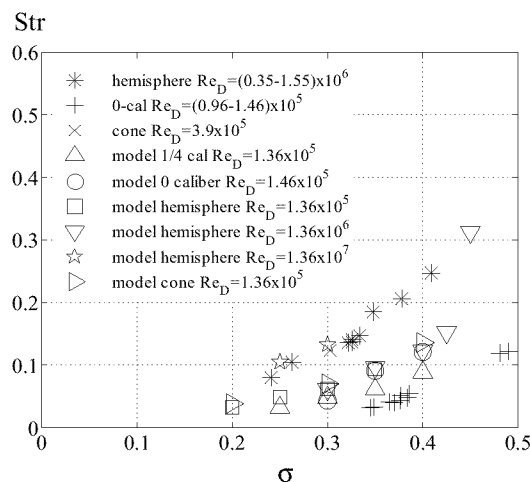


Figure 24. Axisymmetric running cavitators with cylindrical afterbodies. Strouhal frequency and cavitation number. Model results (open symbols) and data reported in Stinebring 36.

Another result found in the  $Str$  versus  $\sigma$  plot (Figure 24) is the tendency of the modeled flows to become steady at higher cavitation numbers. For the 0-caliber or the conical cavitators, this is the reason model results are not included for cavitation numbers greater than 0.4. For the modeled hemisphere, the upper limit of cavitation number to yield unsteady model results was found to be Reynolds number dependent. At a  $Re_D = 1.36 \times 10^5$ , the maximum cavitation number yielding an unsteady result was  $\sigma \approx 0.35$ , at  $Re_D = 1.36 \times 10^6$ , that number was  $\sigma \approx 0.45$ , and at  $Re_D = 1.36 \times 10^7$ , the maximum cavitation number for unsteady computations was not determined. This result may indicate a limit of the computational grid applied to the problems rather than a limit of the level of physical modeling. In addition, physically in the mode of unsteadiness present, a transition does occur from cavity driven to separated, turbulent, but single phase driven flow.

For the conical forebody, the datum shown in Figure 24 suggests that the cycling frequency should be higher, 0.123. It is worth considering that the Reynolds number of the experimental flow was  $3.9 \times 10^5$  and that the general trend with increasing Reynolds numbers is to increased frequency. However, based on the standard level of dependence of Strouhal frequency (see Schlichting [31] for example) on Reynolds number for bluff body flows, it would seem unlikely that the rate of change in frequency with Reynolds number (at  $Re_D \approx 10^5$ ) would be as high as three to two. In addition, compared to shapes with geometrically smooth surfaces, the nature of unsteady flow over a conical shape is not expected to be nearly so dependent on Reynolds number. In the case of a cone, at low values of cavitation number (i.e.  $\sigma = 0.3$ ), the separation location, and, hence, the likely forward location of the cavity, is rarely in question.

A trend that is captured in the model results but not represented in the experimental data included here, is the tendency for the Strouhal frequency of a given cavitator shape to exhibit two distinct flow regimes. The first regime exists at moderate cavitation numbers and is indicated by a low Strouhal frequency where the value of  $Str$  will have an apparent linear dependence on  $\sigma$ . The second regime tends toward much higher cycling frequencies. Here the dependent Strouhal frequency appears to asymptotically approach a vertical line with higher cavitation number, just prior to the complete elimination of the cavity. This is documented in Stinebring [36] and demonstrated in Figure 24 for the modeled hemisphere at  $Re_D = 1.36 \times 10^6$ . Based on the model results, it appears that this is characteristic of a change from a flow mode dominated by a large unsteady cavity to one dominated by other, single-phase, turbulent, sources of unsteadiness.

During this investigation, some effort towards the establishment of temporal and spatial discretization independence was made. As a requirement of the model, to accommodate the use of wall functions, for regions of attached liquid flow, fine-grid near-wall points were established at locations yielding  $10 < y^+ < 100$ .

Temporal convergence was established by the successive reduction of time integration step for several



selected cases. Figure 25 contains a comparison of the spectral content of results for flow over a hemispherical forebody and cylindrical afterbody, with  $Re_D=1.36 \times 10^5$  and  $\sigma=0.3$ , for three, successively smaller, integration step sizes. Here, with a physical time step,  $\Delta t = 0.005$  seconds, the computation resulted in a Strouhal frequency,  $Str=0.0680$ , with a time step,  $\Delta t = 0.0025$  seconds,  $Str=0.0622$ , and with  $\Delta t = 0.001$  seconds,  $Str=0.0680$ . More significantly, as demonstrated in the figure, for the smaller two integration step sizes, over the range of relevant (shown) frequencies, there was very similar modal behavior.

Unfortunately only the fine-grid models tended to provide unsteady results. Thus time and spatial fidelity were judged independently. A demonstration of the steady-state spatial convergence of the modeled conical forebody and cylindrical afterbody is given in Figure 5.

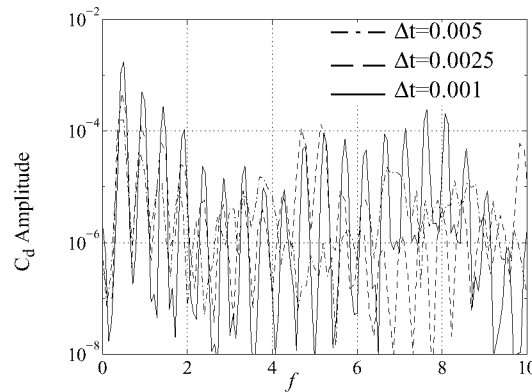


Figure 25. Spectral comparison of effect of physical integration time step size on  $C_d$  history. Flow over a hemispherical forebody with cylindrical afterbody.  $Re_D=1.36 \times 10^5$ .  $\sigma=0.3$ .

### Three-Dimensional Analyses

#### Natural Cavitation about 1/2- and 1-Caliber Ogives

In order to demonstrate the three-dimensional capability of the method, a model of the hemispherical forebody configuration studied above was run at numerous angles of attack and a cavitation number of 0.3. A  $97 \times 33 \times 65$  mesh was utilized (corresponding to the “medium” mesh size discussed in grid studies above). The domain was decomposed into 8 subdomains azimuthally and run on 8 SGI RS10K Octane machines. Parallel efficiencies of 85% were achieved for these problems.

Figure 26 provides sample results for angles of attack of  $0.0^\circ$ ,  $2.5^\circ$ ,  $5.0^\circ$  and  $7.5^\circ$ . These plots include pressure contours on the plane of symmetry, sample streamlines and the cavitation bubble shape as identified with an isosurface of  $\alpha_t = 0.99$ . Several interesting features are observed in the predictions. In particular, the flows are seen to be highly three-dimensional in nature at angle-of-attack. A recirculation zone aft of the bubble, grows with angle of attack. This diminishes the local pressure recovery associated with the bubble-induced blockage and this in turn leads to a local collapse of the bubble on the top of the body. Indeed at angle-of-attack the bubble is seen to have its greatest axial extent off of the symmetry plane of the geometry.

Figure 27 shows the results of a three-dimensional simulation of cavitating flow over a 1-caliber ogive forebody with cylindrical afterbody at a  $10^\circ$  angle-of-attack. A cavitation number of 0.32 was specified. Again a  $97 \times 33 \times 65$  mesh was utilized, the domain was decomposed into eight subdomains azimuthally and run on eight processors and at this cavitation number using this grid a steady state solution could be obtained. Figure 27 illustrates the predicted bubble shape and streamline pattern for this simulation. The bubble shape is highly three-dimensional in nature; it does not close on the pressure side of the body. The streamline pattern is characterized by a large recirculation zone aft of the bubble and significant azimuthally oriented vortical struc-

tures.

Figure 28 shows the convergence history for this case. A three order-of-magnitude drop in the axial velocity residual is achieved in 800 pseudo-time-steps. It is observed that the 8-block/8-processor simulation exhibits nearly identical convergence behavior to a 1-block/1-processor run.

### **Interaction of a Control Surface with Phase-Separated Non-condensable Gas and Liquid Impingement Streams**

The second three-dimensional simulation presented is that of a wedge shaped control surface interacting with an incoming stream of phase-separated water and air. This configuration was tested by the fourth author in the 12" water tunnel at the Penn State Applied Research Laboratory (unpublished). The test was run with co-directed air and water streams. Air was injected along the bottom of the tunnel such that the unperturbed gas-liquid interface impinged upon the sharp leading edge at about 25% span from the base of the fin. Air and water velocities were approximately the same. The configuration was tested at a range of angles-of-attack.

A 189,546 vertex grid was used for the results presented here. The simulation was run on 16 processors with a  $10^\circ$  angle-of-attack and a cavitation number of 0.15. Using this relatively coarse mesh and the k- $\epsilon$  model, a steady-state solution was obtained, despite the presence of a blunt trailing edge and its associated recirculation zone along the span. As we refine our analyses of this class of application, time accurate simulations using upwards of  $10^6$  nodes will be required.

These flows are characterized by several physical features of academic and practical interest. At angle-of-attack, the liquid and gas streams are turned through approximately the same angle, but because the density ratio is high ( $\approx 1000$  here), significant spanwise pressure gradients arise along the lifting surfaces. Accordingly, on the pressure side, the gas-liquid interface is deflected downward, giving rise to deceleration and acceleration of the liquid and gas streams respectively. On the suction surface the lower pressure in the liquid gives rise to an upward deflection of the gas interface. Attendant to these interface deflections is a loss in lift.

Adjacent to the sharp leading edge on the suction side, the local static pressure becomes low due to leading edge separation. Local natural cavitation occurs, and this vapor merges with the swept up non-condensable interface so that the entire suction side is enveloped in gas phase. Aft of the blunt trailing edge, the flow is recirculating and therefore the local static pressure is also low. This gives rise to a sweeping up of the pressure side cavity and some natural cavitation so that the entire wake region is principally gas phase.

Figure 29 shows an oblique front/top view of the predicted flow field. Each of the flow features discussed above is clearly observed in the simulation. Of particular note is that the three-species formulation enables the separate prediction and identification of vaporous and non-condensable regions of the flow. Figure 30a shows a suction side video frame of the tested flow configuration at this angle-of-attack. The enveloping of the suction surface in gas phase and the primarily gas phase wake are observed. Figure 30b shows a pressure side photograph. A similar view of the simulation is presented in Figure 30c which shows that the pressure surface interface deflection and gas-vapor wake region are qualitatively consistent with experimental observation.

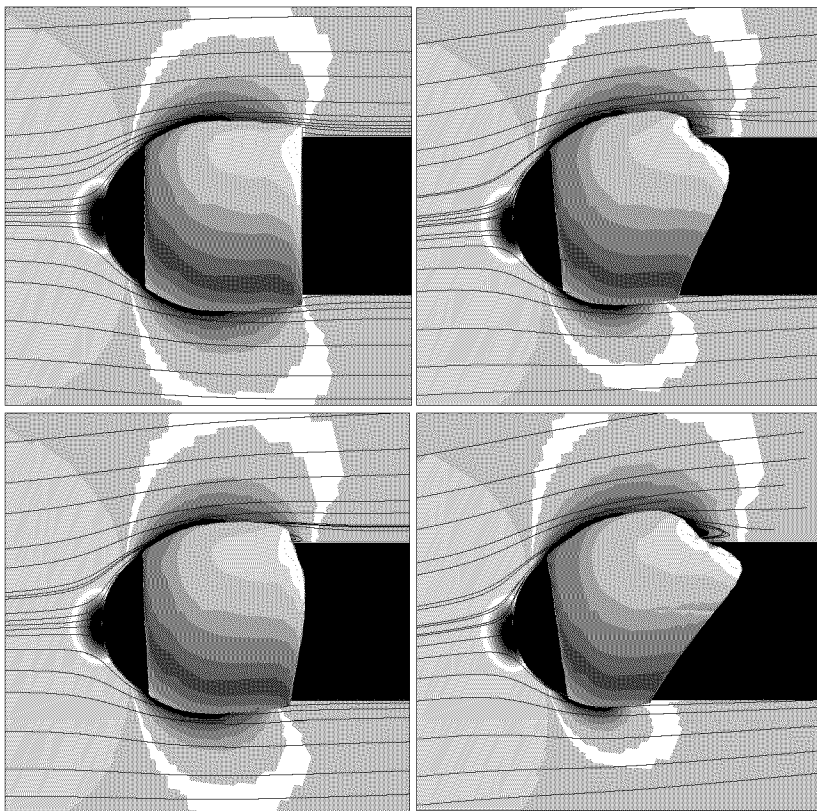


Figure 26. Predicted 3-D flow field with natural cavitation about hemispherical fore-body at several angles of attack.  $\sigma = 0.3$ . Liquid volume fraction = 0.99 isosurface.

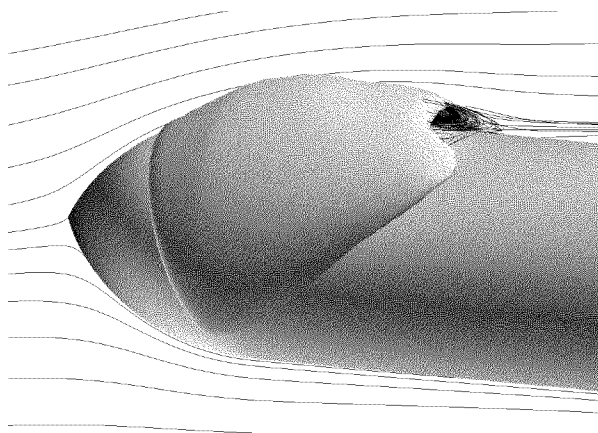


Figure 27. Predicted bubble shape (designated by  $\alpha_t = 0.99$  isosurface) and streamlines for a 1-caliber ogive at a  $10^\circ$  angle-of-attack.

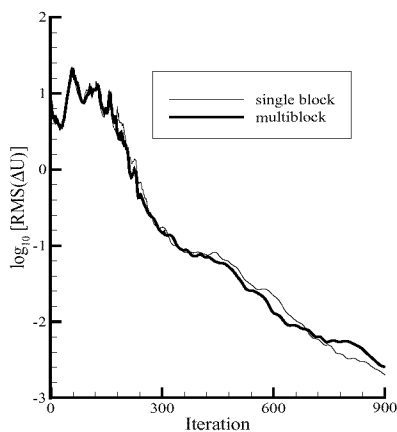


Figure 28. Comparison of 1-block/1-processor and 8-block/8-processor convergence histories for a 1-caliber ogive at a  $10^\circ$  angle-of-attack.

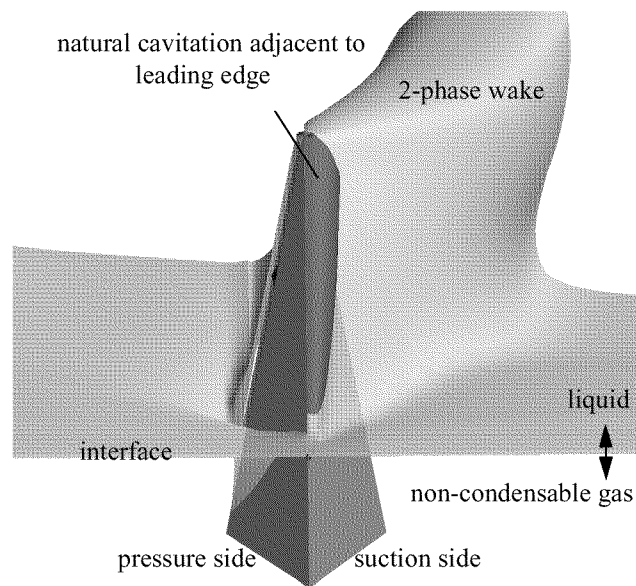


Figure 29. Front/top view of CFD simulation of supercavitating fin configuration at  $10^\circ$  angle-of-attack. Isocontours of  $\alpha_{ng} = 0.9$ ,  $\alpha_v = 0.9$  designate non-condensable gas and vapor regions respectively.

### Three-dimensional Flow over a Vehicle with Ventilation and Natural Cavitation

Practical high speed supercavitating vehicle designs employ ventilation at or near the cavitator leading edge, where natural cavitation will likely also occur. Figure 31 illustrates elements of a 48-processor three-dimensional analysis of a notional vehicle with natural cavitation, noncondensable gas injection and propulsion stream. This illustrates the three-species nature of the formulation.

### Unsteady Three-Dimensional Flow Over a 0-Caliber Ogive

As pointed out by Edwards [10], a potential cause of the discrepancies observed between predicted and measured Strouhal numbers for the cavitator series simulations is the axisymmetric nature of the unsteady runs. We have begun to investigate this by simulating these flows three-dimensionally. Figure 32 illustrates elements of a 1,245,184 cell, 78 processor unsteady simulation of flow over a blunt ogive at  $\sigma=0.30$ .  $Re_D=1.46 \times 10^5$ . Clearly observable are non-axisymmetric predicted cavity shapes. We continue to investigate these modes in the hope of quantifying them.

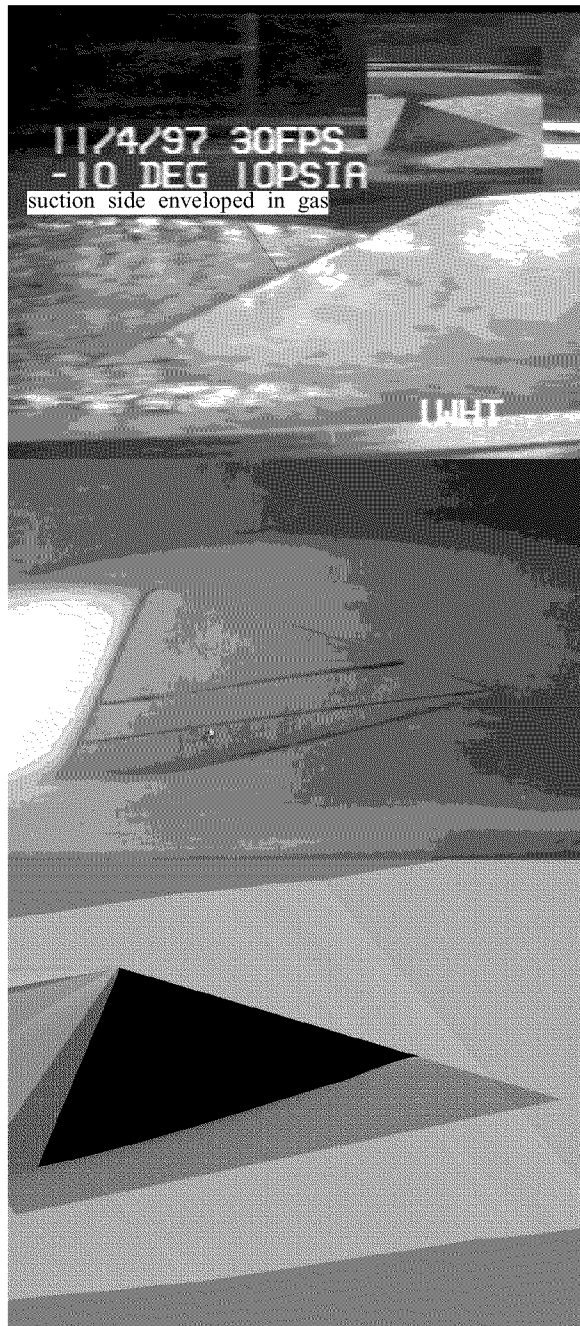


Figure 30. a) Suction side video frame of super-cavitating fin at  $10^\circ$  angle-of-attack. b) Pressure side photograph. c) Pressure side view of CFD simulation.

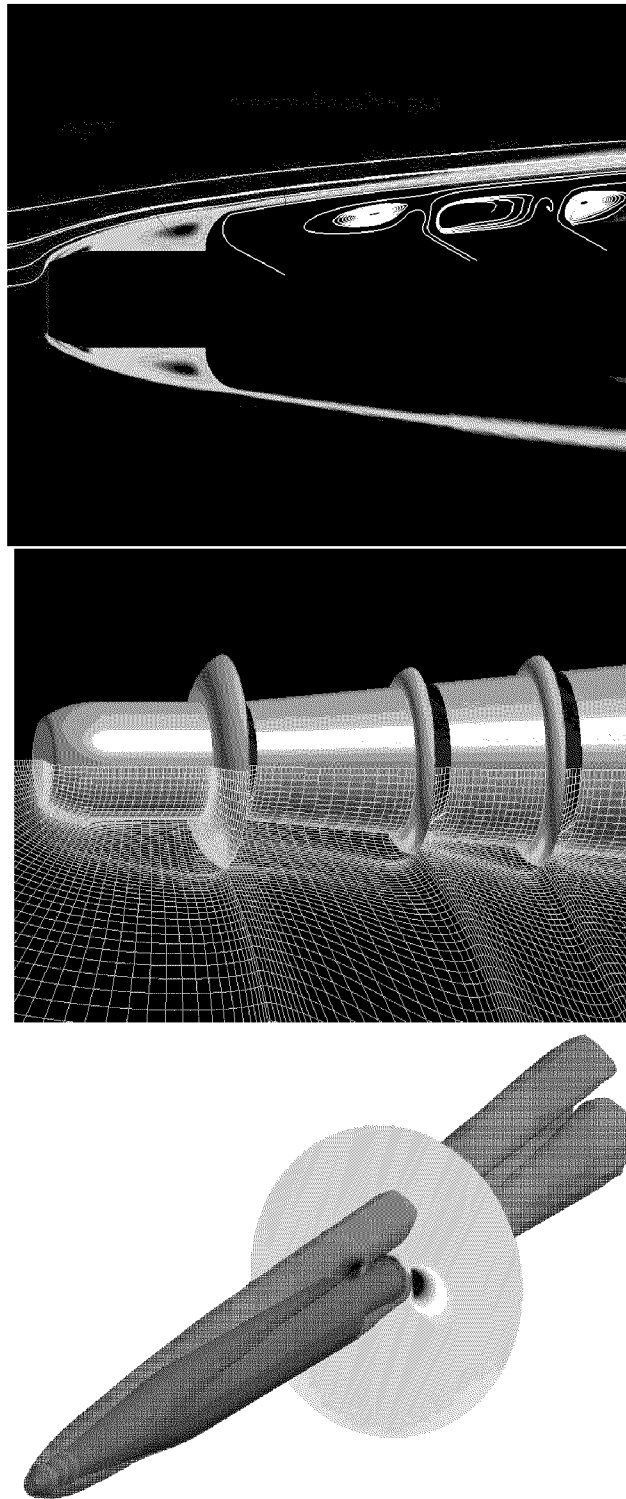


Figure 31. Elements of three-dimensional supercavitating vehicle simulations with ventilated and natural cavitation. a) liquid volume fraction contours and stream lines ( $\alpha = 0^\circ$ ), b) view of 3D geometry and grid, c) liquid volume fraction = 0.9 isovolume and vertical velocity contour plane ( $\alpha = 5^\circ$ ).

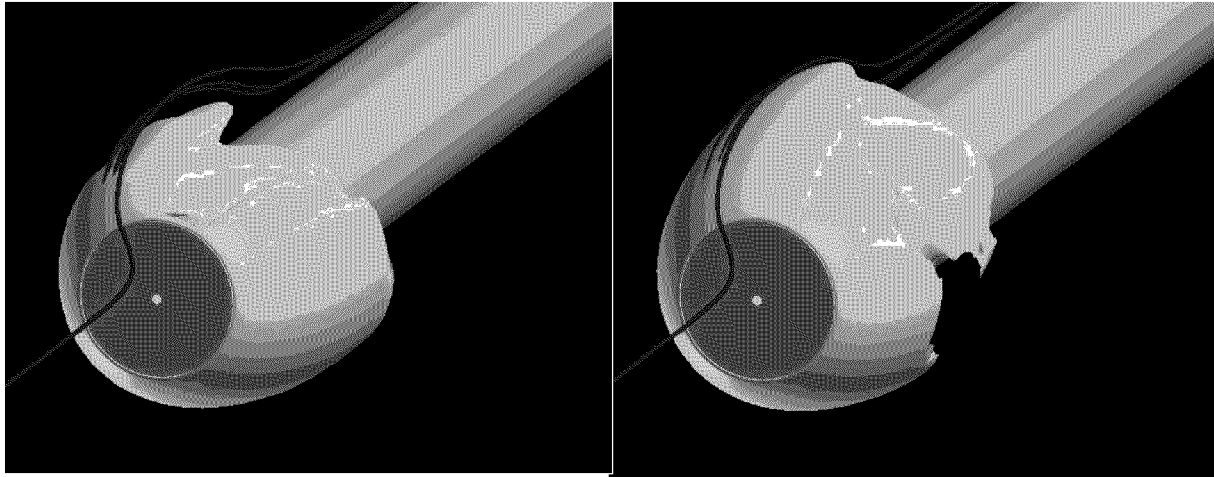


Figure 32. Three-dimensional, turbulent, unsteady, two-phase result. 1,245,184 cell grid. Flow over blunt ogive with an isosurface of volume fraction,  $\alpha_l=0.9$ , and selected streamlines at two timesteps.  $\sigma=0.30$ .  $Re_D=1.46 \times 10^5$ .

### Sheet Cavitation in a Centrifugal Pump

The authors have recently extended our efforts towards the analysis of sheet cavitation in turbomachinery. Some representative results are presented here. Figure 33 shows three simulations of a generic backswept impeller at three cavitation numbers. These plots show a front view of the impeller, with surface pressure contours on the blade surfaces and hub. Also shown are the predicted sheet cavities on the blade surfaces as designated with an isovolume contour of liquid volume fraction = 0.9. A single blade passage was computed; the results have been copied several times to yield a complete annulus view.

We have not yet analyzed the cavitation *performance* of this three dimensional configuration. This is because when employing the higher order convection differencing and fine grids required for accurate cavitation bubble size predictions for a specified cavitation number, the cavities and thereby the simulation are unsteady. As a step towards the goal of predicting cavitation performance in pumps, we have analyzed a quasi-three-dimensional midspan streamsheet representation of the same configuration. Performance predictions for this series of analyses are shown in Figure 34. In Figure 34a, head coefficient versus flow coefficient is plotted for a spectrum of flow coefficients and cavitation numbers. Single phase results are plotted as solid red diamonds. A characteristic head drop off is observed off design (though clearly efficiency levels and off design trends are unrealistic due to the quasi-three-dimensional modeling employed). A sequence of successively lower cavitation numbers were run for several flow coefficients. The reduction in predicted head attendant to the sheet cavitation are also plotted in Figure 34a. Figure 34b illustrates the ability of the analysis to capture incipient cavitation breakdown physics. There, head coefficient is plotted versus cavitation number for the series of quasi-three-dimensional simulations. At each flow coefficient, a rapid drop-off in head is observed at a critical cavitation number.

The authors point out that these pump cavitation results are preliminary and several issues remain to be resolved including the need for improved mass transfer modeling to account for thermal effects on cavitation breakdown, and three-dimensional performance analysis.

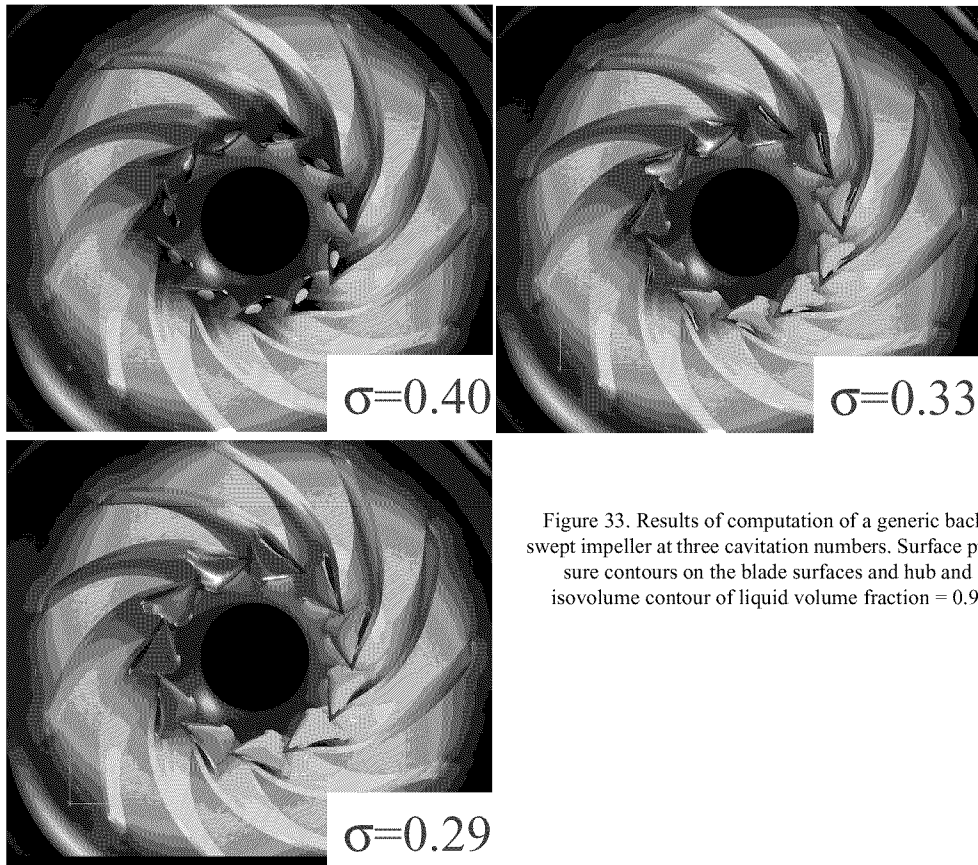


Figure 33. Results of computation of a generic back-swept impeller at three cavitation numbers. Surface pressure contours on the blade surfaces and hub and isovolume contour of liquid volume fraction = 0.9.



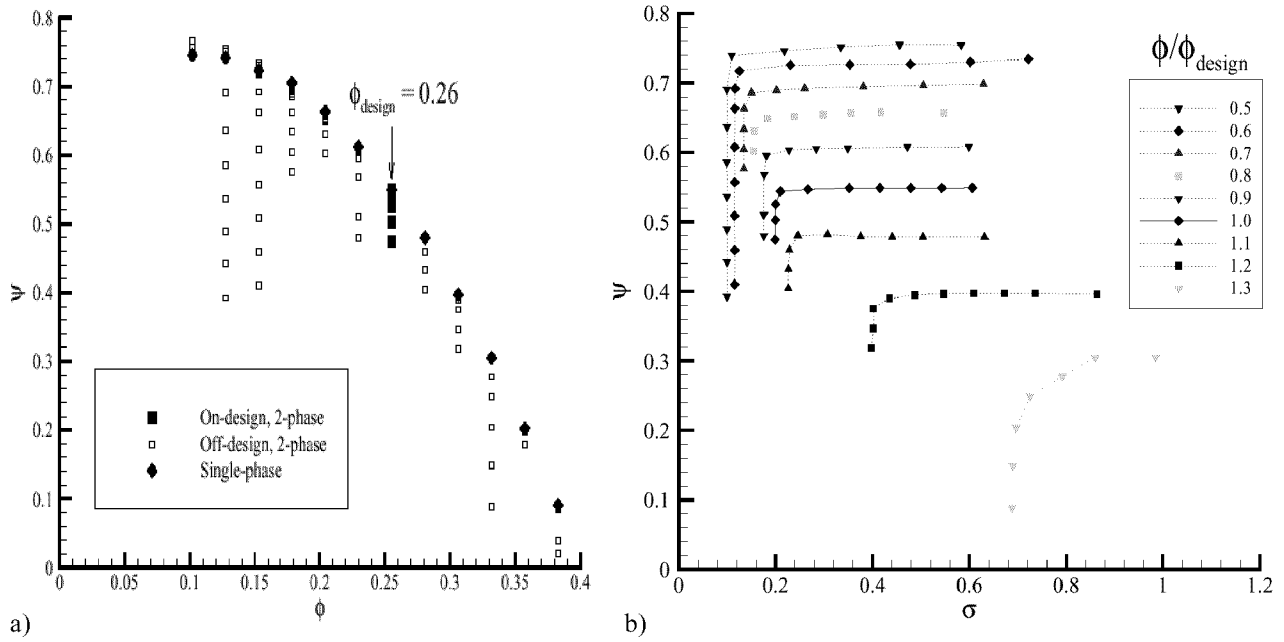


Figure 34. Results of quasi-three-dimensional midspan streamsheet analyses of a generic backswept impeller. a) predicted efficiency vs. flow coefficient, b) predicted head coefficient vs. cavitation number at several flow coefficients.

### Compressible Simulations

Some recently obtained compressible flow results are presented in Figures 35 and 36. Figure 35 contains an illustrative result of a projectile traveling supersonically relative to the speed of sound in water. On the left is a photograph of the actual test. At right is the model result for this case. In the model result, the liquid to vapor density ratio is nominally 1000, and the Mach Number is 1.03. The example is illustrative of challenging modeling issues. In the liquid flow, there are shock waves. These are resolved with MUSCL interpolation and the van Albada limiter. In addition, due to the high flow velocity, the cavitation index is approximately  $10^{-4}$ . In the figure, dark blue indicates density of less than one and red indicates density of nominally 1000. Thus, most of the flow immediately adjacent to the object is completely vaporized as is the downstream wake. This is exhibited in both the photograph and the model result.

Figure 36 contains a modeled axisymmetric plume from a hypothetical rocket operating underwater. Here the jet is supersonic and slightly underexpanded. It is surrounded by a second gas stream which is subsonic (notionally the vehicle cavity) and finally by a subsonic water free stream. In this case the nominal liquid to gas density ratio is again 1000. In the density field, red indicates a density of nominally 1000, and blue indicates a density of one or less. In the shock function field, the classic expansion pattern followed by shocks are exhibited. The interaction of the compressible gas stream with the nearly incompressible liquid is demonstrated by the contraction and expansion, from top to bottom in the figure, of the gas stream. In addition, the interface between the gas and liquid contains fully supersonic flow. This region is highlighted by the shock function due to the density gradient, but does not necessarily contain shocks. A line segment drawn locally normal to the interface would be nearly isobaric. Further results of our compressible multiphase efforts are available in [20] and [41].

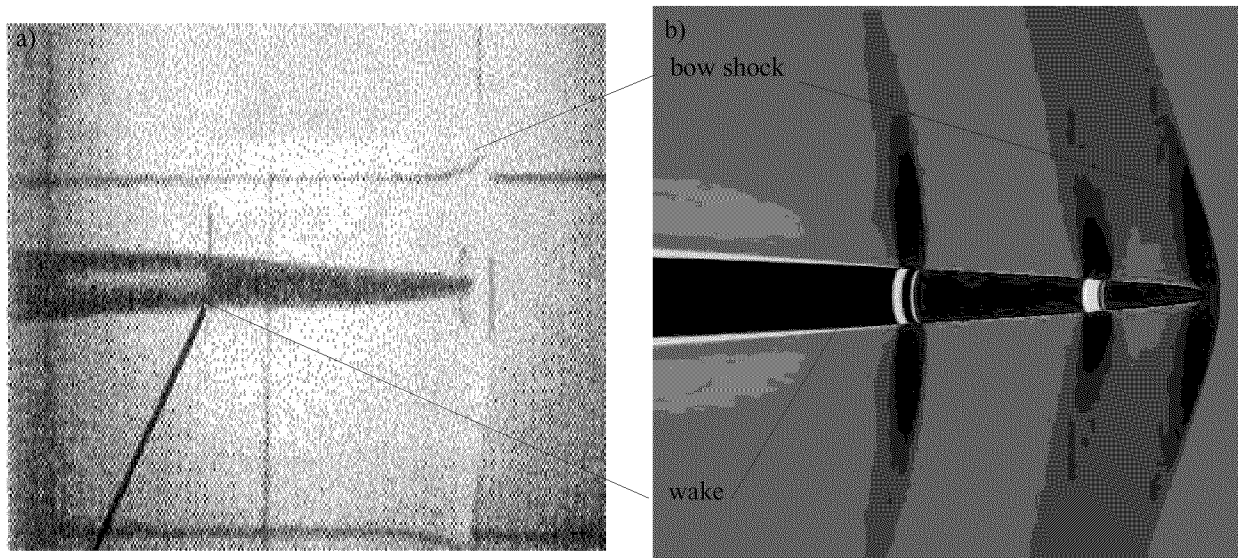


Figure 35. Hypervelocity projectile test and computation. a) Photograph of a projectile at  $M=1.03$  with respect to water sound speed. b) Corresponding simulation showing surface pressure and field mixture density contours.

## Conclusions

A multi-phase CFD method has been presented and applied to a number of high density ratio developed- and super-cavitating flows. Several aspects of the method were outlined and demonstrated that enable convergent, accurate and efficient simulations of these flows. These include a differential model and preconditioning strategy with favorable eigensystem characteristics, a block implicit dual-time solution strategy, a three species formulation that separately accounts for condensable and non-condensable gases, higher order flux differencing with limiters and the embedding of this scheme in a parallel multi-block Navier-Stokes platform.

The two-dimensional/axisymmetric simulations presented verify the ability of the tool to accurately analyze steady-state and transient sheet- and super-cavity flows. The three-dimensional and compressible capability of the code was demonstrated as well.

As the authors proceed with this research, we are focusing on several areas including: 1) validation of the method for compressible constituent fields, 2) improved physical models for mass transfer and turbulence, 3) extended application and validation for steady and transient three-dimensional flows and 4) improved error damping through preconditioning and pseudo-time-stepping formulations that locally adapt to problem parameters.

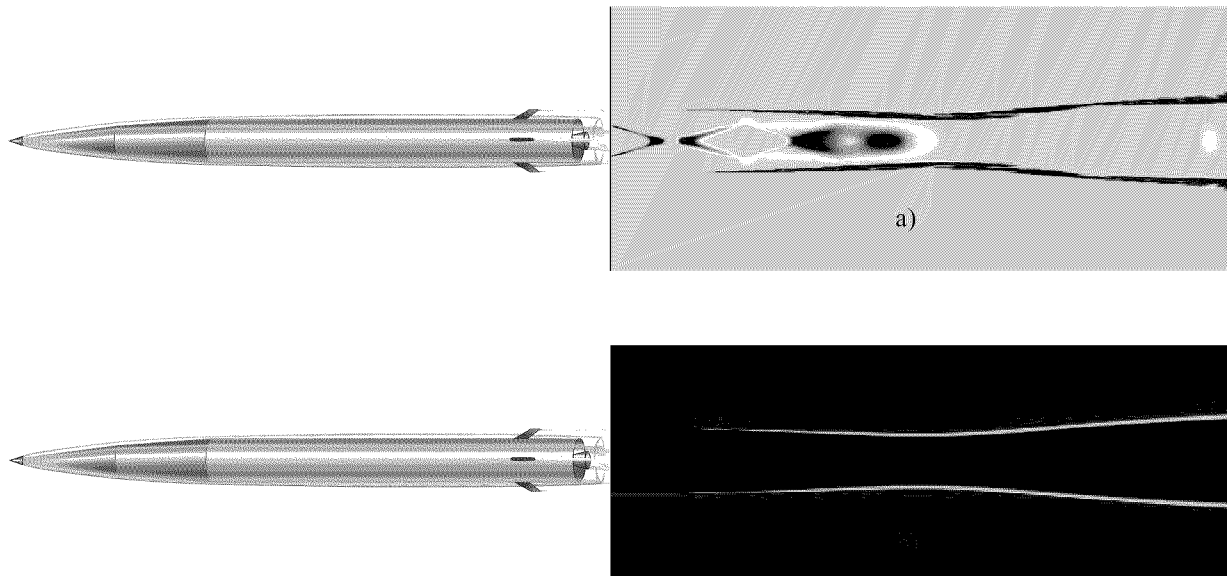


Figure 36. Cartoon vehicle and 3-stream, axisymmetric plume computation. Center jet (diameter=1,  $M=3$  with respect to propellant sound speed) surrounded by cavity gas at free stream velocity (outer diameter=2,  $M \ll 1$ ), surrounded by freestream liquid (Liquid to gas density ratio 1000,  $M \ll 1$ ). a) mixture density contours, b) shock function,  $\mathbf{v} \cdot \nabla p$ , contours.

## Acknowledgments

This work is supported by the United States Office of Naval Research with Dr. Kam Ng as contract monitor. This work was supported in part by a grant of HPC resources from the Arctic Region Supercomputing Center and in part by a grant of SGI Origin 2000 HPC time from the DoD HPC Center, Army Research Laboratory Major Shared Resource Center.

## References

1. Ahuja, V., Hosangadi, A., Ungewitter, R., Dash, S.M. (1999) "A Hybrid Unstructured Mesh Solver for Multi-Fluid Mixtures, AIAA Paper 99-3330.
2. Anderson, W.K., Thomas, J.L., Van Leer, B. (1986) "Comparison of Finite Volume Flux Vector Splittings for the Euler Equations," *AIAA Journal*, Vol. 24, No. 9, pp.1453-1460.
3. Arndt, R., Song, C., Kjeldsen, M., He, J., Keller, A. (2000) "Instability of Partial Cavitation: A Numerical/Experimental Approach", presented at the 23rd Symposium on Naval Hydrodynamics, Val de Reuil, France.
4. Brennan, C.E., *Cavitation and Bubble Dynamics*, Oxford University Press, New York, 1995.
5. Brennan, C.E., *Hydrodynamics of Pumps*, Oxford University Press, England, 1994.
6. Chen, Y., Heister, S.D. (1994) "Two-Phase Modeling of Cavitated Flows," ASME FED-Vol. 190, pp.299-307.
7. Chorin, A.J. (1967) "A Numerical Method for Solving Incompressible Viscous Flow Problems," *Journal of Computational Physics*, Vol. 2, pp. 12-26.
8. Dellanoy, Y., Kueny, J.L. (1990) "Two-phase Flow Approach in Unsteady Cavitation Modeling," ASME FED-Vol. 98, pp.153-158.
9. Dieval, L., Pellone, C., Arnaud, M. (2000) "Advantages and Disadvantages of Different Techniques of Modeling of Supercavitation," Proceedings of Meeting on High Speed Hydrodynamics and Supercavitation, Grenoble, France.
10. Edwards, J.R. (2000) Published discussion to reference [19].
11. Garabedian, P.R. (1958) "Calculation of Axially Symmetric Cavities and Jets," *Pac. J. of Math* 6.
12. Grogger, H.A., Alajbegovic, A., (1998) "Calculation of the Cavitating Flow in Venturi Geometries Using Two Fluid Model," ASME Paper FEDSM 98-5295.

13. Hirsch, C. (1990) Numerical Computation of Internal and External Flows, Volume 2, John Wiley and Sons, New York.
14. Jameson, A., Schmidt, W., Turkel, E. (1981) "Numerical Solutions of the Euler Equations by Finite Volume Methods Using Runge-Kutta Time-Stepping Schemes," AIAA Paper 81-1259.
15. Kirchner, I. N. (2001) "Numerical Modeling of Supercavitating Flows," VKI Special Course on Supercavitating Flows, February.
16. Jones, W.P., Launder, B.E. (1972) "The Prediction of Laminarization with a Two-Equation Model of Turbulence," *International Journal of Heat and Mass Transfer*, Vol. 15, pp. 301-314.
17. Kunz, R.F., Siebert, B.W., Cope, W.K., Foster, N.F., Antal, S.P., Eitorre, S.M (1998) "A Coupled Phasic Exchange Algorithm for Three-Dimensional Multi-Field Analysis of Heated Flows with Mass Transfer," *Computers and Fluids*, Vol. 27, No. 7, pp. 741-768.
18. Kunz, R.F., Boger, D.A., Stinebring, D.R., Chyczewski, T.S., Lindau, J.W., Gibeling, H.J., Venkateswaran, S., Govindan, T.R. (1999) "A Preconditioned Navier-Stokes Method for Two-Phase Flows with Application to Cavitation Predication," AIAA Paper 99-3329, also *Computers and Fluids*, Vol. 29, No. 8, [Nov, 2000], pp. 849-875.
19. Lindau, J.W., Kunz, R.F., Gibeling, H.J. (2000) "Validation of High Reynolds Number, Unsteady Multi-Phase CFD Modeling for Naval Applications," presented at the 23rd Symposium on Naval Hydrodynamics, Val de Reuil, France.
20. Lindau, J.W., Kunz, R.F., Venkateswaran, S., Boger, D.A. (2001) "Application of a Preconditioned, Multiple-Species, Compressible, Navier-Stokes Model to Cavitating Flows", Submitted to the 4th International Symposium on Cavitation, Pasadena, California, 20-23 June.
21. Lindau, J.W., Venkateswaran, S., Kunz, R.F., Merkle, C.L. (2001) "Development of a Fully-Compressible Multi-Phase Reynolds-Averaged Navier-Stokes Model", AIAA Paper 2001-2648.
22. May, A. (1975) "Water Entry and the Cavity-Running Behaviour of Missiles," Naval Sea Systems Command Hydroballistics Advisory Committee TR-75-2.
23. Merkle, C.L., Feng, J., Buelow, P.E.O. (1998) "Computational Modeling of the Dynamics of Sheet Cavitation," Proceedings of 3rd International Symposium on Cavitation, Grenoble, France, pp. 307-311.
24. Orszag, S.A., Yakhot, V., Flannery, W.S., Boysan, F., Choudhury, D., Maruzewski, J., Patel, B. (1993) "Renormalization Group Modeling and Turbulence Simulations, Near Wall Turbulent Flows," Elsevier Science Publishers B.V., Amsterdam, The Netherlands.
25. Reboud, J. L., Delannoy, Y. (1994) "Two-Phase Flow Modeling of Unsteady Cavitation," Proceedings of 2nd International Symposium on Cavitation, Tokyo, Japan, pp. 39-44.
26. Reboud, J. L., Fortes-Patella, R., Hofman, M., Lohrberg, H., Ludwig, G., Stoffel, B. (1999) "Numerical and Experimental Investigations on the Self-Oscillating Behaviour of Cloud Cavitation," ASME Paper FEDSM99-7259, Proceedings of 3rd ASME/JSME Joint Fluids Engineering Conference.
27. Reichardt, H. (1946) "The Laws of Cavitation Bubbles at Axially Symmetrical Bodies in a Flow," Ministry of Aircraft Production Volkenrode, MAP-VG, Reports and Translations 766, Office of Naval Research.
28. Rogers, S. E., Chang, J. L. C., Kwak, D. (1989) "A Diagonal Algorithm for the Method of Pseudocompressibility," *Journal of Computational Physics*, Vol. 73, pp. 364-379.
29. Rouse, H., McNown, J. S. (1948) "Cavitation and Pressure Distribution, Head Forms at Zero Angle of Yaw," Studies in Engineering, Bulletin 32, State University of Iowa.
30. Saurel, R., Cocchi, J.P., Butler, P.B. (1999) "Numerical Study of Cavitation in the Wake of a Hypervelocity Underwater Projectile," *AIAA Journal of Propulsion and Power*, Vol. 15, No.4, pp. 513-520.
31. Schlichting, H. (1979) Boundary-Layer Theory, McGraw-Hill, New York.
32. Shin, B.R., Ikohagi, T. (1998) "A Numerical Study of Unsteady Cavitating Flows," Proceedings of 3rd International Symposium on Cavitation, Grenoble, France, pp. 301-306.
33. Shyy, Wei (2000) Personal communication and published discussion to reference [19].
34. Siebert, B.W., Maneri, C. C., Kunz, R.F., Edwards, D. P. (1995) "A Four-Field Model and CFD Implementation for Multi-Dimensional, Heated Two-Phase Flows," 2nd International Conference on Multiphase Flows, Kyoto, Japan.
35. Song, C., He, J., (1998) "Numerical Simulation of Cavitating Flows by Single-Phase Flow Approach," Proceedings of 3rd International Symposium on Cavitation, Grenoble, France, pp. 295-300.
36. Stinebring, D.R., Billet, M.L., Holl, J.W. (1983) "An Investigation of Cavity Cycling for Ventilated and Natural Cavities," TM 83-13, The Pennsylvania State University Applied Research Laboratory.
37. Stinebring, D.R. (1976) "Scaling of Cavitation Damage," M.S. Thesis, The Pennsylvania State University, University Park, Pennsylvania, August.
38. Stinebring, D.R., Billet, M.L., Lindau, J.W., Kunz, R.F. (2001) "Developed Cavitation-Cavity Dynamics," VKI Special Course on Supercavitating Flows, February.
39. Taylor, L. K., Arabshahi, A., Whitfield, D. L. (1995) "Unsteady Three-Dimensional Incompressible Navier-Stokes
40. Venkateswaran, S., Deshpande, M., Merkle, C.L. (1995) "The Application of Preconditioning to Reacting Flow

- Computations,” AIAA Paper 95-1673, from Proceedings of the 12th AIAA Computational Fluid Dynamics Conference.
41. Venkateswaran, S., Lindau, J.W., Kunz, R.F., Merkle, C.L. (2001) “Evaluation of Preconditioning Algorithms for the Computation of Multi-Phase Mixture Flows,” AIAA Paper 2001-0279.
  42. Venkateswaran, S., Merkle, C. L. (1995) “Dual Time Stepping and Preconditioning for Unsteady Computations,” AIAA Paper 95-0078.
  43. Van der Heul, D.R., Vuik, C., Wesseling, P. (2000) “Efficient Computation of Flow with Cavitation bay Compressible Pressure Correction”, Proceedings of AMIF-ESF Workshop on Computing Methods for Two-Phase Flow, Aussois, France.
  44. Vasin, A. (2000) “High Speed Body Motion in Compressible Fluid,” Proceedings of Meeting on High Speed Hydrodynamics and Supercavitation, Grenoble, France.
  45. Whitfield, D. L., Taylor, L. K. (1994) “Numerical Solution of the Two-Dimensional Time-Dependent Incompressible Euler Equations,” Mississippi State University CFD Laboratory Report MSSU-EIRS-ERC-93-14.